

Understanding the Role of Voxel Size on Large Vein Contamination in BOLD Functional MRI

Undergraduate Honours Thesis
PHYS 4909
Winter 2025

Haydn Flemming
Student ID: 101101446

Supervisor: Dr. Berman

April 2025

Contents

1	Introduction	2
2	Theory	3
2.1	MR Theory	3
2.2	Equilibrium Magnetization	3
2.3	RF Excitation and Flip Angle	4
2.4	Relaxation	5
2.5	Gradient Echo 'Apparent' Transverse Relaxation (T_2^*)-weighted images . . .	7
2.6	MR Image Encoding and Slice Selection	8
2.7	Voxel Size and SNR	9
2.8	Susceptibility Artefacts	10
2.9	The BOLD Effect and BOLD fMRI	11
2.10	Vessel-Size Sensitivity	13
2.11	BOLDswimsuite	14
3	Methods	18
3.1	BOLDswimsuite Toolbox Modifications	18
3.1.1	Tissue Index	18
3.1.2	Anisotropic Voxel Sizes	20
3.1.3	Sub-Voxel Sampling	20
3.2	Simulation Building	21
3.2.1	Simulation parameters	23
3.3	Sub-Voxel Sampling	25
4	Results	26
4.1	Simulated Signal Visualization	26
4.2	Signal Integration and Difference Plot	27
4.3	Finding the Critical Depth	29
5	Discussion	34
6	Conclusion	34
7	References	35
8	Appendices	38
8.1	Signal Plots	38
8.2	Integral Plots	39
8.3	Percent Signal Change Plots	40
8.4	Critical Depth Plots	41

1 Introduction

Blood Oxygenation Level Dependent (BOLD) functional Magnetic Resonance Imaging (fMRI) leverages variations in blood oxygenation levels in the brain to create contrast, providing a non-invasive tool for mapping brain activity. The signal amplitude and contrast of BOLD fMRI are influenced by several factors, including voxel size and signal saturation from large veins. These factors limit the spatial specificity of the BOLD signal, limiting its ability to precisely map neuronal activity.

The purpose of this project is in understanding the role of voxel size and position in BOLD signal contamination by large veins. Recent work in ultra-high field MRI has produced small fMRI voxel sizes (500-micron scale) with the ability to detect neuronally-driven activation [44]. Small voxel sizes provide increased imaging resolution and a reduction in physiological noise and related instabilities. These smaller voxel sizes may also improve microvascular specificity in gradient-echo BOLD [16].

Field inhomogeneities produced by a large vein dominate the BOLD signal over a small imaging area, as shown in Figure 1, a 2D model of the effect of large vein contamination in mesoscopic field inhomogeneities.

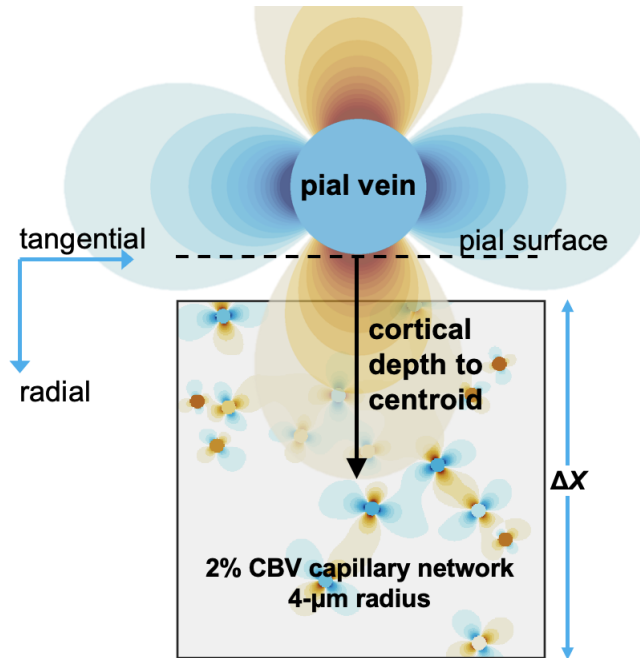


Figure 1: An illustration of mesoscopic field inhomogeneities caused by a Pial vein. Also displayed is a 2D voxel showing the field offset generated by capillaries [18].

This study aims to model the effect of large vein signal contamination in BOLD contrast. This will be explored by constructing a 3D representation of the brain’s vasculature, approximated using “infinite” cylinders. The magnetic field offsets produced by this vasculature will then be calculated using both discrete (FFT-based) and analytical methods. To model the full BOLD response, proton spin behavior will be simulated under an applied RF pulse, followed by diffusion modeling to capture the effects of spin dephasing on total voxel

signal. This approach enables a detailed investigation of how large veins influence signal loss and contrast in BOLD fMRI.

2 Theory

2.1 MR Theory

When a strong static magnetic field is applied to a sample, it aligns the magnetic moments of nuclei with non-zero spin angular momentum, inducing a net magnetization in the sample [23]. MR images are then produced by using a pulse sequence, which consists of radiofrequency (RF) pulses and gradient pulses, to tip the net magnetization away from the longitudinal axis into the transverse plane. The transverse component of the magnetization then induces a voltage in a receiver coil, the basis of MR signal [10]. MRI primarily exploits the magnetic properties of hydrogen nuclei in the body. Two important properties that impact the signal intensity from different tissues in MRI include proton density (PD) and characteristic times for magnetization to relax if perturbed from equilibrium [1].

A simple classification will be used to describe bodily tissues that produce different types of contrast: **Fluids**, which consists of cerebrospinal fluid (CSF), synovial fluid, and oedema, **water-based tissues**, which consists of muscle, brain, cartilage, and kidney, and **fat-based tissues**, which consists of fat and bone marrow. Each classification has different contrast (signal intensity) on MR images, allowing the visualization of tissue boundaries [2].

Proton density is related to the number of hydrogen atoms in a volume. Relaxation time refers to the time it takes for tissue to return to equilibrium after an RF pulse. Fluids typically have a longer T_1 , (1500-2000ms), water-based tissues have a shorter T_1 , (400-1200ms), and fat-based tissues generally have the shortest T_1 , (100-150ms). For any given tissue, T_2 will be shorter than T_1 . T_2 follows a similar trend to T_1 , with fluids having the longest relaxation time (700-1200ms) and water-based tissues generally having longer T_2 times than fat-based tissues, (40-200ms) and (10-100ms) respectively. MR image contrast is generally dependent on either PD, T_1 , or T_2 [1].

2.2 Equilibrium Magnetization

When a nucleus has non-zero spin angular momentum, it possesses a magnetic moment μ due to its intrinsic charge and spin, given by

$$\mu = \gamma S \tag{1}$$

where γ is the gyromagnetic ratio of the nucleus, and S is the spin angular momentum.

When a static magnetic field B_0 is applied to nuclear spins, the spins will precess about the direction of the field. The frequency of this precession is proportional to the strength of the applied field, given by the **Larmor equation** below.

$$\omega_o = \gamma B_0 \tag{2}$$

Where ω_o is equal to the precessional frequency. The gyromagnetic ratio for protons is $\gamma = 2.7 \times 10^8 \text{ rad s}^{-1} \text{ T}^{-1}$. In the presence of a static magnetic field, a majority of nuclear

spins will tend to align with the field. Quantum mechanics describes this behavior as an increased probability that a nucleus will occupy the lower energy state, which corresponds to μ and B_0 being parallel.

In a volume of nuclei, the sum of individual magnetic moments give the net magnetization of the system, M_0 , governed by the equation below.

$$M_0 = \frac{1}{V} \sum_N \mu_i \quad (3)$$

Where V is the system volume and N the number of nuclei within it [24]. Figure 2 below shows a diagram of protons, which exist in either a parallel or anti-parallel state, aligned with or oppositely aligned with the static magnetic field B_0 . Combining their magnetic moments results in an equilibrium net magnetization aligned in the direction of the field, referred to as the longitudinal magnetization.

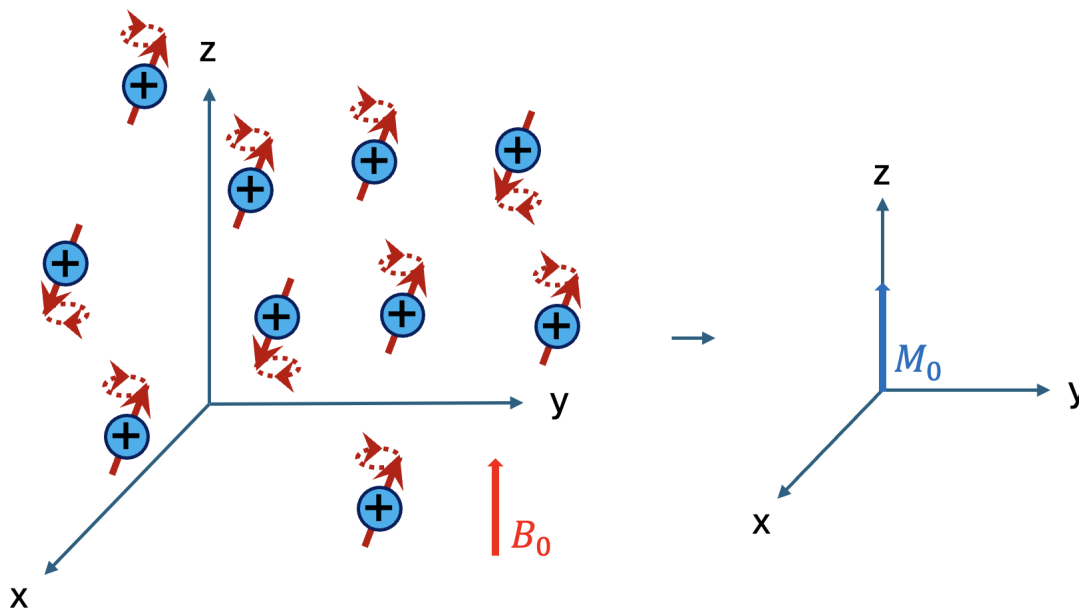


Figure 2: The combined net magnetization (M_0) resulting from the precession of many protons aligned with an external magnetic field.

2.3 RF Excitation and Flip Angle

It is difficult to measure the longitudinal magnetization while it is aligned with the static magnetic field. If the static field is defined along the z-axis, the longitudinal magnetization will also align with this axis. An RF pulse can be used to tip the longitudinal magnetization into the x-y plane, referred to as the transverse plane, allowing for the induction of a measurable signal in a receiver coil aligned with this plane. Figure 3 below shows an illustration of the tipping of the precession of the longitudinal magnetization into the transverse plane.

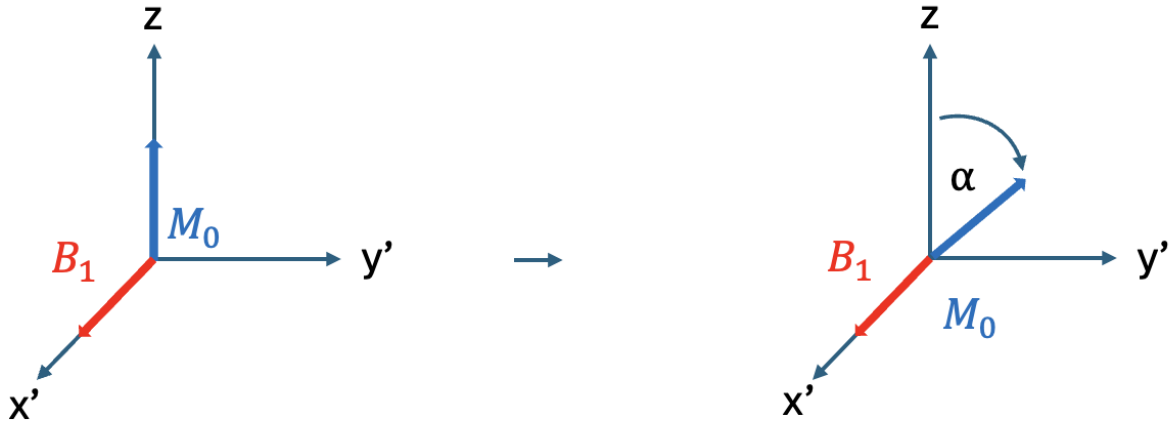


Figure 3: The magnetic field B_1 produced by an RF pulse on the transverse plane illustrating the resulting precession of the longitudinal magnetization with flip angle α .

The angle of precession of the longitudinal magnetization is proportional to the strength and duration of the RF field. For example, if a 180° flip angle was desired, the strength of the RF field would be increased. The equation below shows the flip angle α .

$$\alpha = \gamma B_1 t_p \quad (4)$$

Where γ is the gyromagnetic ratio, B_1 is the strength of the RF magnetic field, and t_p is the length of time the pulse is applied for. In MRI, it is common to change the strength or duration of the RF pulse to produce different flip angles [10].

2.4 Relaxation

The relaxation times, T_1 and T_2 , are both intrinsic tissue properties. T_1 describes the time constant at which the longitudinal magnetization returns to its initial maximum value, given by:

$$M_z = M_0 \left(1 - \exp \left(-\frac{t}{T_1} \right) \right) \quad (5)$$

Where M_z is the longitudinal component of the net magnetization [38]. T_2 describes the time constant at which the transverse magnetization decays, given by:

$$M_{xy} = M_0 \exp \left(-\frac{t}{T_2} \right) \quad (6)$$

Where M_{xy} is the transverse component of the net magnetization [39].

Susceptibility effects in patients create imperfect, inhomogeneous magnetic fields. These effects arise due to air pockets in the sinuses or intestines, dense bone at the skull base, and iron-rich blood breakdown products, among other sources [3]. These susceptibility differences distort the surrounding magnetic field, causing nearby tissues to experience local magnetic

field inhomogeneities [41]. In a gradient echo sequence, the combination of susceptibility effects with the generation of an imperfect magnetic field produced by an MRI machine results in a sped up transverse relaxation time, named the 'apparent' relaxation time (T_2^*). A comparison in signal intensity between the 'true' T_2 from a perfect homogeneous magnetic field with no susceptibility effects present in tissue and T_2^* resulting from an MRI machine with both a high quality, more homogeneous magnetic field, and low quality, less homogeneous field is shown below in figure 4 [3].

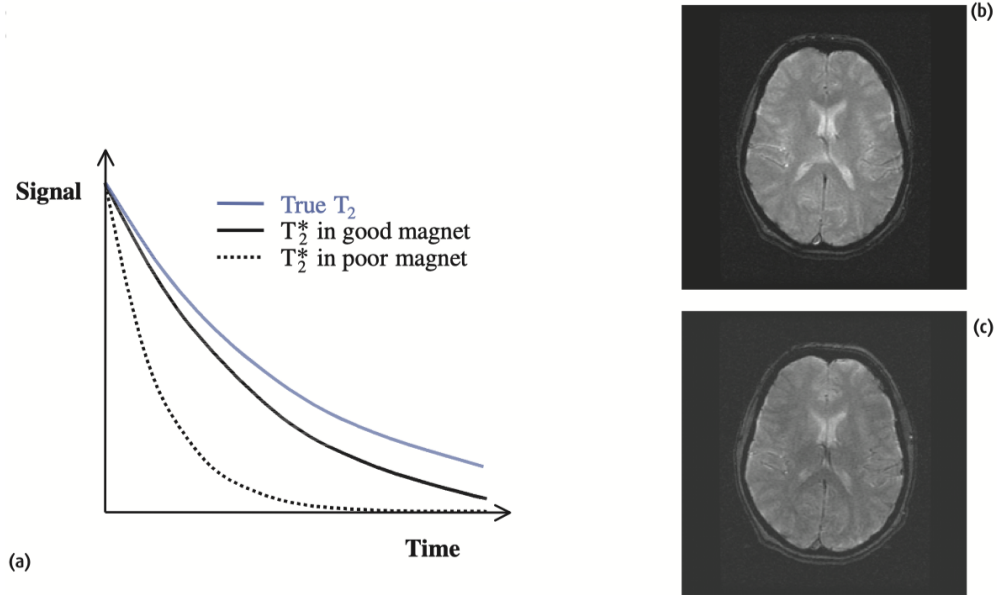


Figure 4: (a) A comparison of signal intensity between T_2 and T_2^* , showing the influence of magnetic field uniformity on signal decay. Images (b) and (c) show MR images acquired under different magnetic field homogeneity conditions. Image (b) was obtained with a high quality magnet, while (c) was acquired with artificially reduced field homogeneity, demonstrating the impact of shortened T_2^* on signal intensity and image contrast [4].

In T_2 weighted images, contrast is proportional to T_2 . Long T_2 values appear brighter than shorter T_2 values, and improved field homogeneity can enhance signal to noise ratio and, depending on the specific image features of interest, may improve contrast [5]. This can be seen in figure 4, where (b) has a more homogeneous magnetic field than (c), resulting in better contrast.

The observed transverse relaxation rate (R_2^*) is the rate of decay of the transverse magnetization. It is used to represent how quickly a signal decays in a gradient-echo sequence.

$$R_2^* = \frac{1}{T_2^*}$$

The main difference between R_2^* and T_2^* is that R_2^* describes the decay process in terms of rate, while T_2^* describes the time it takes for the process to occur. The traditional expression for R_2^* is shown below.

$$R_2^* = R_2 + R_2' \tag{7}$$

Where R_2 is the transverse relaxation rate,

$$R_2 = \frac{1}{T_2}$$

and R_2' is the additional rate caused by magnetic field inhomogeneities [19]. While R_2^* and T_2^* are directly related, R_2^* is useful in describing the rate of signal decay in modeling applications.

2.5 Gradient Echo 'Apparent' Transverse Relaxation (T_2^*)-weighted images

The two common types of pulse sequences are called spin echo (SE) and gradient echo (GE). The focus of this paper is on gradient echo pulse sequences. The GE pulse sequence use a single radiofrequency pulse followed by magnetic field gradient pulses, used for spatial encoding. This creates the echo, which is also a measure of signal intensity [1].

In the gradient echo sequence, an RF excitation pulse is applied initially. A negative gradient lobe is applied after the excitation pulse, shown in figure 5. This intentionally causes the transverse magnetization to more rapidly decay. After this, a positive gradient is applied to reverse the magnetic field gradient. This causes the previously dephasing spins to rephase, resulting in the signal seen at the echo, given by the equation below.

$$S_{GE} = S_o \exp\left(-\frac{TE}{T_2^*}\right) \quad (8)$$

Where S_{GE} is the height of the echo, S_o is the initial height of the signal, described by free induction decay, echo time (TE) is the time when spins are rephased following the excitation, and T_2^* is the apparent relaxation time [11].

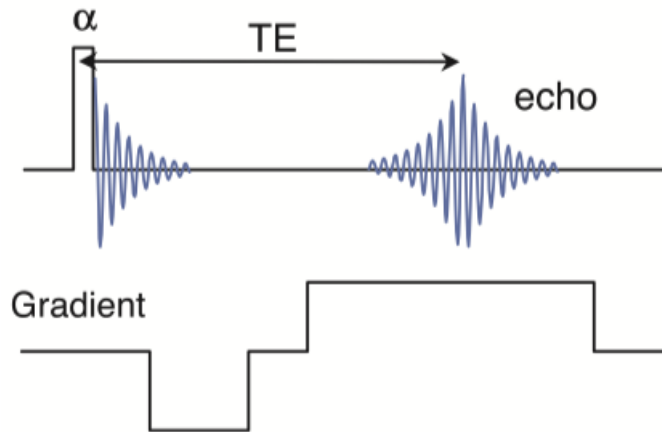


Figure 5: A sample gradient echo pulse sequence, with gradient showing the magnitude and direction of the applied gradient pulse, α displaying the flip angle, and TE representing the echo time [12].

2.6 MR Image Encoding and Slice Selection

Signal alone is not sufficient to produce an image in MRI; spatial information must also be encoded to determine where within the imaging volume the signal originated. This is achieved through the use of magnetic field gradients applied in different directions during the pulse sequence.

One gradient is used for slice selection, allowing for the excitation of a specific cross-sectional plane in the imaging volume. The position, thickness, and orientation of the slice can all be controlled. This process involves a specially designed RF pulse applied at the same time as the gradient pulse. This RF pulse contains a narrow range of frequencies centered around the Larmor frequency [21].

The resulting digitized MR signal is stored in k-space, a representation of the image in the frequency-domain. The two spatial encoding directions of k-space are the frequency encode (FE) axis and phase encode (PE) axis. During each acquisition, one full line of k-space is sampled along the FE direction, while the PE gradient is incremented to fill k-space line by line [26]. Once these signals are collected, a Fourier transform is applied to convert k-space, the spatial frequency domain, into a spatial distribution of excited nuclei, forming an image of the volume. The signal intensity of each pixel in the resulting image relates to the MR signal strength of the corresponding voxel in the imaging volume [27].

Central data in k-space contains signal-to-noise and contrast information, with an illustration of this below in figure 6.

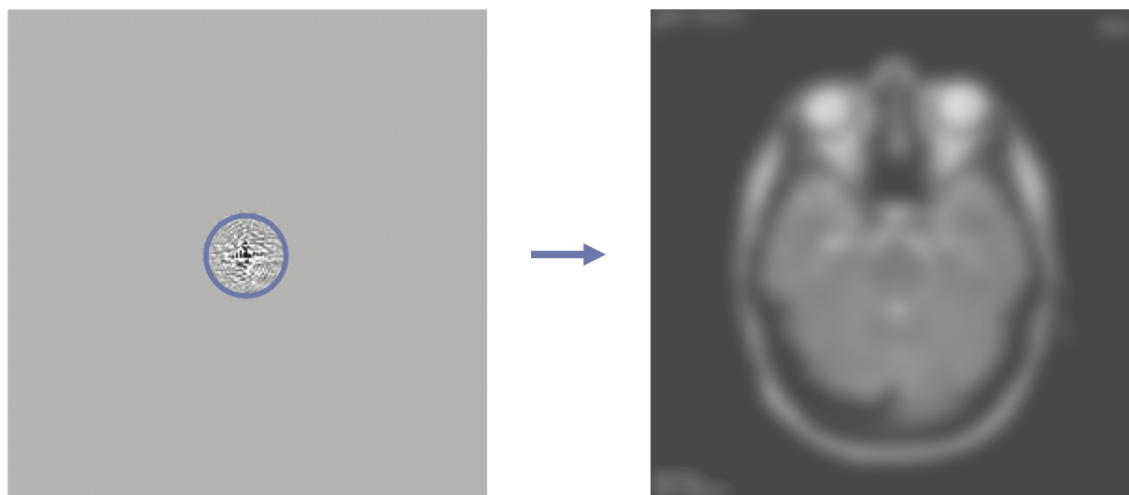


Figure 6: A reconstruction of the central data in k-space, revealing only signal and contrast information in the resulting image [25].

Data surrounding the center of k-space contains all information about the image resolution, with an example shown below in figure 7.

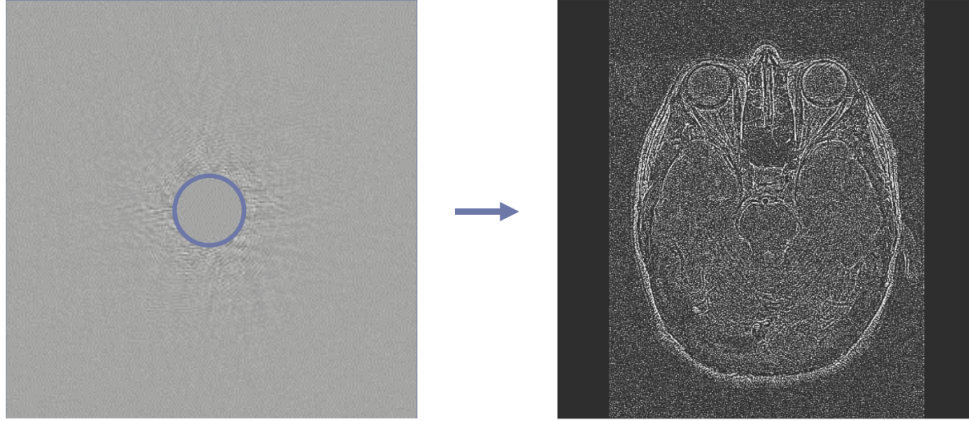


Figure 7: A reconstruction of k-space with the middle removed, showing tissue boundaries but a low signal-to-noise ratio and no contrast information [25].

2.7 Voxel Size and SNR

Each pixel in an MRI image corresponds to a volume element, or voxel, within the larger imaging volume. The pixel represents the front face of the voxel, with its depth defined by the slice thickness. In the case that a voxel contains multiple tissue types, the resulting signal will be the weighted sum of the signals from each tissue. Figure 8 below shows an illustration of both a voxel derived from a 2-D image, along with a distribution of voxels across multiple slices in a patient [28].

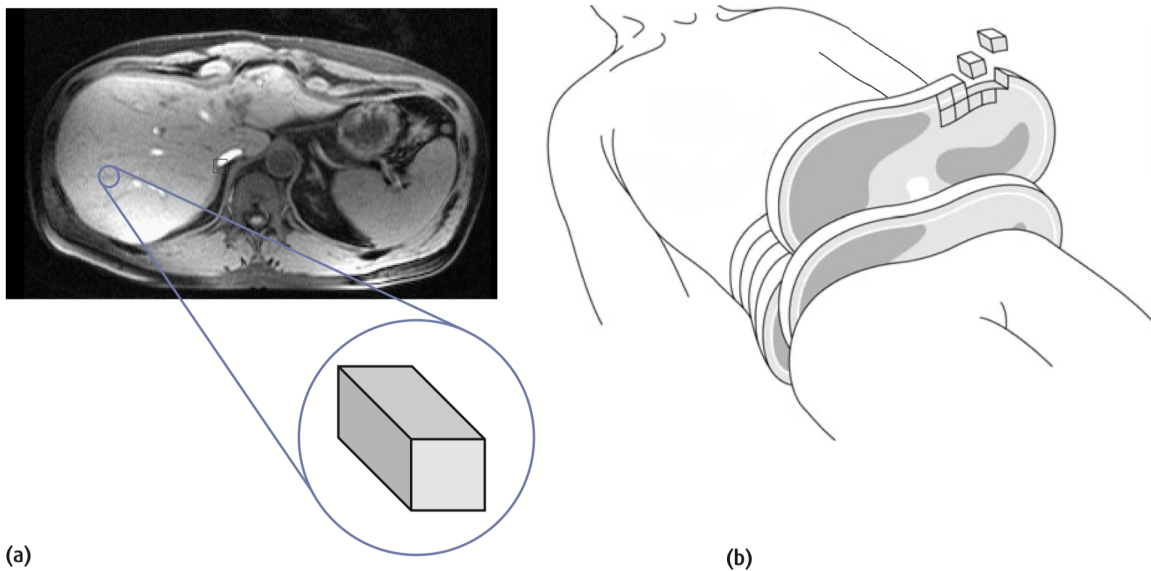


Figure 8: (a) A voxel representing the volume element behind a 2D pixel in an image. (b) A patient divided into slices, with those slices divided into a grid of separate voxels [29].

Individual voxels that make up an MR image will represent a mixture of both signal and noise. The ratio of signal intensity to background noise is known as the signal-to-noise

ratio (SNR). With a low SNR, subtle contrast changes may be lost, and structural details can be obscured. An equation describing SNR is shown below:

$$\text{SNR} \propto \frac{\Delta x \cdot \Delta y \cdot \Delta z \cdot F_{\text{sequence}} \cdot \sqrt{\text{NSA} \cdot N_{\text{PE}}}}{\sqrt{bw}} \quad (9)$$

Where Δx and Δy are the pixel dimensions, Δz is the slice thickness, and F_{sequence} is a factor that describes how the pulse sequence and tissue relaxation properties affect signal strength. NSA is the number of signal averages (i.e., the number of times a k-space line was repeated and averaged), N_{PE} is the number of phase encoding steps, and bw is the bandwidth per pixel.

Assuming constant scan time and acquisition parameters, this relationship shows that SNR is directly proportional to voxel volume [30]. However, SNR also depends on the strength of the static magnetic field. Increasing the magnetic field strength leads to a higher net magnetization, allowing for a higher SNR [31, 42]. As a result, for a given voxel size at one field strength, an unacceptable level of noise may be present in an image. At a higher field strength, some of the lost SNR may be recovered, potentially making the image usable.

2.8 Susceptibility Artefacts

Susceptibility artefacts arise when tissues become magnetized to different extents in the static magnetic field due to variations in magnetic susceptibility [41]. This causes macroscopic field inhomogeneities at the boundaries between tissues, increasing the dephasing of nearby protons. This dephasing leads to a decrease in the signal intensity of local voxels. These artefacts may present as reduced or zero intensity areas of contrast in the resulting images [22].

Figure 9 below shows a depiction of susceptibility artefacts resulting from air-tissue interfaces, demonstrating that thinner slice selection can reduce dephasing.

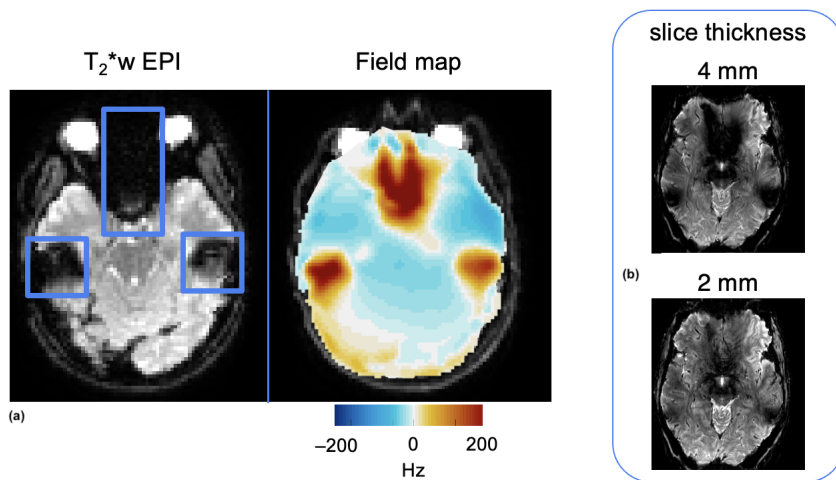


Figure 9: (a) Dephasing from macroscopic field inhomogeneities, seen at air tissue interfaces. (b) The effect of decreased slice thickness on reducing dephasing from macroscopic field gradients [20].

Thinner slice selection reduces dephasing by limiting the range of magnetic field inhomogeneities sampled within each voxel. By acquiring thinner slices, each voxel represents a smaller volume and therefore samples a narrower range of susceptibility-induced magnetic field offsets. This reduces dephasing within the voxel, resulting in higher signal intensity and a reduction in susceptibility artefacts [40].

2.9 The BOLD Effect and BOLD fMRI

The BOLD (Blood Oxygenation Level Dependent) effect arises from differences in magnetic susceptibility between oxyhaemoglobin and deoxyhaemoglobin. While oxygenated blood is diamagnetic, deoxygenated blood is paramagnetic and introduces local magnetic field perturbations in the presence of a static magnetic field. These perturbations increase the dephasing of nearby hydrogen nuclei in the transverse plane, shortening T_2^* and reducing MR signal.

Figure 10 compares veins with high and low oxygen saturation (SO_2), illustrating the stronger magnetic field offset produced by a high concentration of deoxyhaemoglobin. This offset is the primary cause of spin dephasing and the subsequent reduction in MR signal near vessels with low oxygenation.

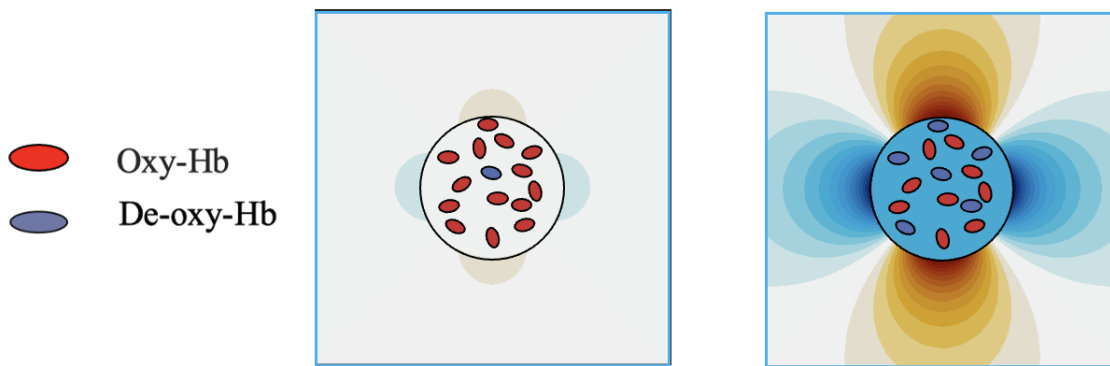


Figure 10: A diagram showing the cross section of an artery (left) with high oxygen saturation, and vein (right) with low oxygen saturation, displaying the difference in magnetic field offset between them [33].

As shown in figure 11, during periods of neuronal activation, increased consumption of oxygen is accompanied by a disproportionate increase in the supply of fully oxygenated blood. At the activation site and downstream from it, the concentration of deoxygenated blood is therefore reduced, resulting in decreased magnetic perturbations, a lengthening of T_2^* , and elevated MR signal [13]. Because the BOLD effect is driven by magnetic susceptibility, its sensitivity increases with magnetic field strength [42]. Additionally, as SNR also improves with increasing field strength, the sensitivity of BOLD signal measurements is enhanced at higher fields [14].

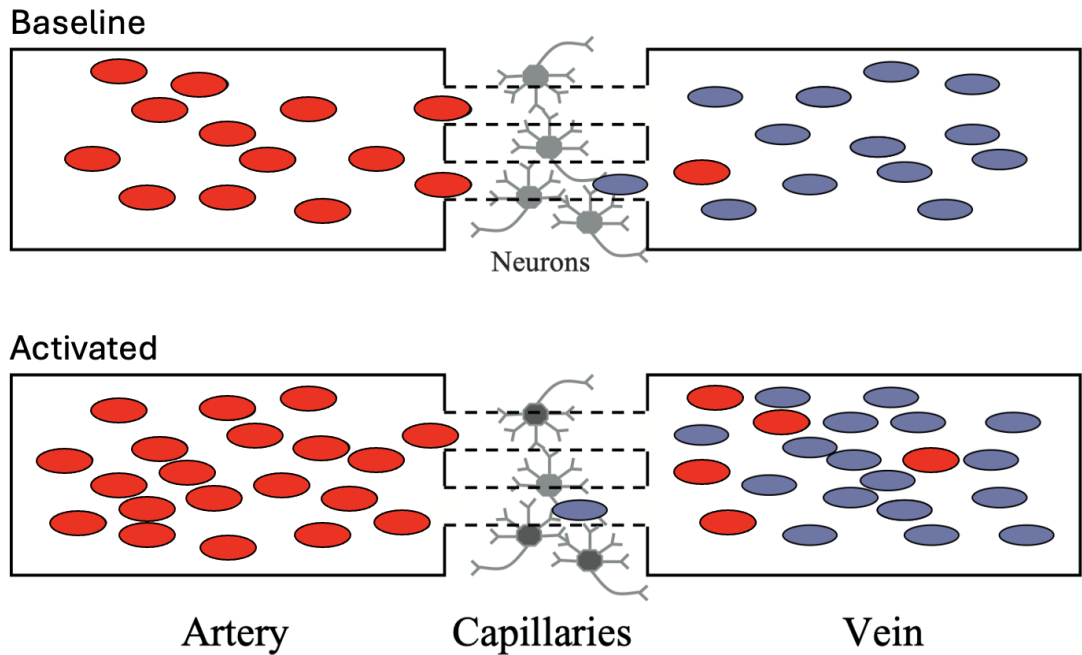


Figure 11: A diagram comparing oxygen saturation at baseline and activation, showing an increase in blood flow and subsequent decrease in concentration of deoxygenated blood downstream from the activation site [32].

Functional MRI (fMRI) is a non-invasive imaging technique used to map brain activity by detecting changes in blood oxygenation. fMRI relies on the BOLD effect to infer neuronal activation from localized fluctuations in MR signal. Figure 12 below shows a sample fMRI activation map generated by comparing baseline MR signal to signal during a visual stimulus. A heatmap overlays regions of statistically significant signal change, with bright areas indicating strong BOLD contrast and localized neuronal activation.

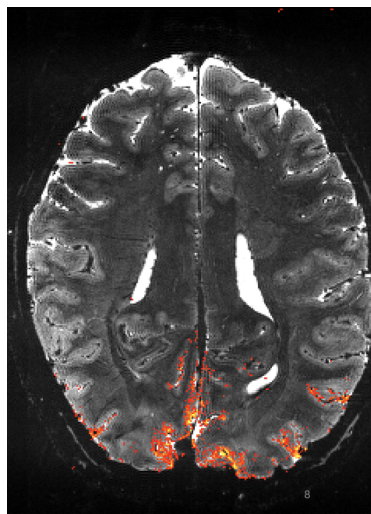


Figure 12: A sample fMRI image, showing a heatmap of neuronal activation during visual stimulation [44].

2.10 Vessel-Size Sensitivity

The sensitivity of BOLD signal is not uniform across vessel sizes. For gradient echo BOLD, the sensitivity is assessed by changes in the apparent transverse relaxation rate (R_2^*). This sensitivity change is primarily caused by the change in diffusion of water molecules through field inhomogeneities, due to the change in magnetic susceptibility between blood and tissue.

There are three primary types of dephasing regimes: motional narrowing, intermediate, or static dephasing. The type of dephasing is dependent on the relative proportion of characteristic diffusion distance and dephasing introduced by magnetic field inhomogeneities. **Motional narrowing** corresponds to the case where diffusion is large compared to the magnetic field inhomogeneities, like in the region surrounding small vessels. **Static dephasing** corresponds to the opposite case, where diffusion is relatively small compared to the magnetic field inhomogeneities present, present in the region surrounding large vessels. The **intermediate dephasing regime** occurs between these extremes.

Figure 13 below shows the relationship between these dephasing regimes and gradient echo (GE) BOLD relaxation rates.

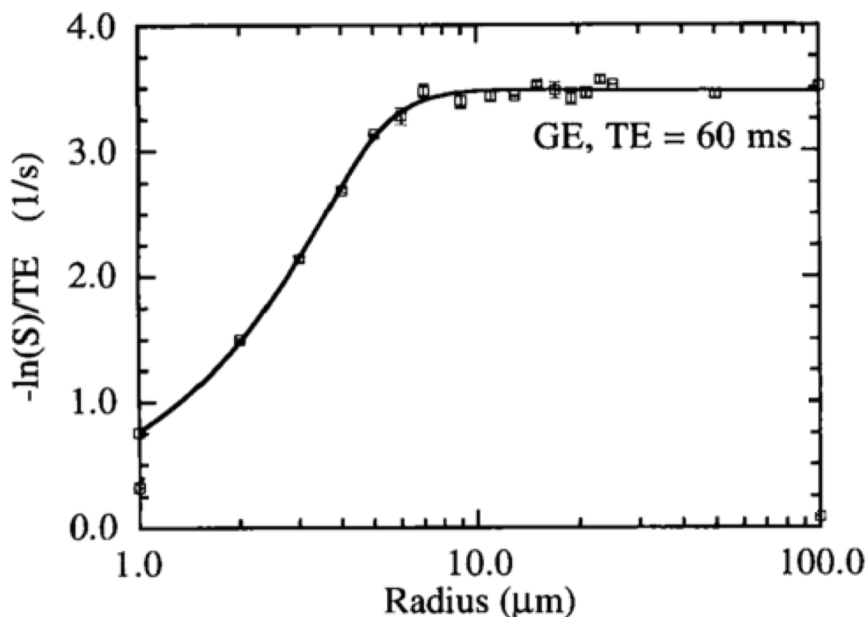


Figure 13: Vessel-size dependence on the effective relaxation rate of gradient echo [35].

This observed dependence of R_2^* on vessel size arises from the increased time individual spins spend in regions of large magnetic field offset as vessel radius increases, leading to faster signal decay. Because of this, GE BOLD is particularly sensitive to blood oxygenation changes in large draining veins, such as on the Pial surface [36].

2.11 BOLDs ω imsuite

The BOLD fMRI technique has become widely used in modern MR imaging. Modeling of the T_2^* -weighted BOLD signal has become a valuable method in understanding both current applications and its origins. BOLDs ω imsuite (Chausse et al., 2024) is a toolbox implemented in Python that makes use of both Monte-Carlo and deterministic diffusion based simulations. It makes use of a range of geometries, used to describe sources of magnetic field perturbations in both 2D and 3D [15].

BOLDs ω imsuite has built in perturber classes for modeling of 3D vessel geometries. The main focus of this paper will be on Infinite cylinders, one of the predefined perturbers modeled in the BOLDs ω imsuite simulation module. Infinite cylinders are defined analytically and are produced using few parameters, defined by the user or generated randomly. The limitation of this model is through the lack of curvature and branching, resulting in mixed degrees of accuracy in the representation of real vasculature. Figure 14 below shows a representation of the 3D infinite cylinders in a populated voxel [15].

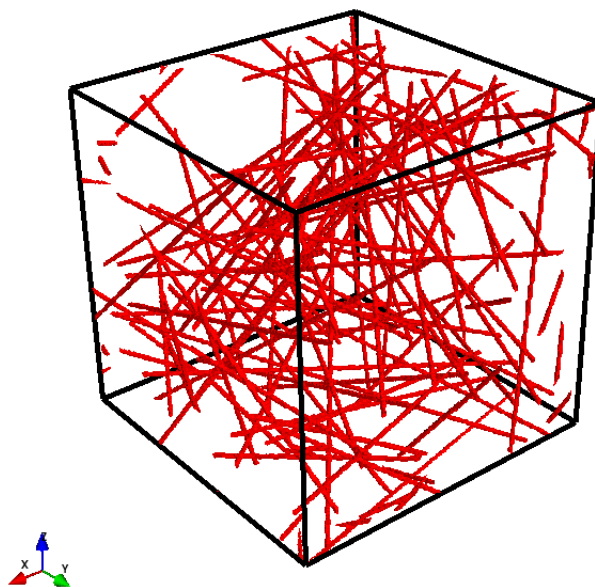


Figure 14: A depiction of a sample voxel, populated by 3D infinite-cylinders.

The diameter, position, orientation, magnetic susceptibility, and water permeation probability define the 3D infinite-cylinders. Parameters are input manually and position and orientation are then randomly generated, resulting in a uniformly distributed cerebral blood volume (CBV), which is the fractional volume of the voxel occupied by vessels, within the voxel. There are two main methods for calculating the magnetic field (B_o) offset in the simulations, either analytically or by FFT convolution [15].

When modeled analytically, the magnetic field offset of infinite-cylinders can be calculated exactly, in either continuous or discrete space simulations. The equation below describes the calculation of the magnetic field offset [34].

$$\Delta B_z = \begin{cases} B_0 \frac{\Delta\chi}{6} (3 \cos^2(\theta) - 1), & \text{inside cylinder} \\ B_0 \frac{\Delta\chi}{2} \left(\frac{R}{r}\right)^2 \cos(2\phi) \sin^2(\theta), & \text{outside cylinder} \end{cases} \quad (10)$$

This describes the magnetic field offsets both inside and outside of each cylinder. B_o is the strength of the applied magnetic field, $\Delta\chi$ is the susceptibility difference between the intra-cylinder and extra-cylinder spaces, R is the radius of the cylinder, r is the magnitude of the distance between the axis of the cylinder and measured spin position, θ is the angle between the cylindrical axis and the applied magnetic field, and ϕ is the angle between the vector \mathbf{r} and the projection of B_o on a plane orthogonal to the cylinder axis [15].

The second method for calculating the magnetic field offset is by discrete Fourier transform. The dipoles local to the perturbations of the field are calculated in the Fourier domain and then transformed back to the spatial domain. The field offsets are calculated in k-space as follows [15]:

$$B_z(\vec{r}) = \mathcal{F}^{-1} \left\{ \mathcal{F}\{\chi(\vec{r})\} \cdot G(\vec{k}) \right\} B_0 \quad (11)$$

Where $B_z(\vec{k})$ is the field offset in k-space, $\chi(\vec{r})$ is the magnetic susceptibility distribution, $G(\vec{k})$ is the kernel that represents the relationship between the magnetic susceptibility distribution and the field offset in the spatial domain expressed in k-space, and B_o is the applied magnetic field. The kernel is expressed in k-space as:

$$G_{z,3D}(\vec{k}) \equiv \mathcal{F}\{G_{z,3D}(\vec{r})\} = \frac{1}{3} - \frac{k_z^2}{k^2} \quad (12)$$

Where $G(\vec{k})$ is the kernel expressed in k-space, $G(\vec{r})$ is the representation of the kernel in the spacial domain, $k = k_x^2 + k_y^2 + k_z^2$ is the wave vector in Fourier space, and k_z is the z-component of the wave vector in Fourier space.

The field offsets resulting from the convolution in equation 11 are inherently discretized. This limits the spatial resolution resulting from the calculation. Another limitation is that the result is susceptible to boundary effects and wrap-around artifacts. These can be avoided by adding zero-padding to the arrays used in the Fourier transforms. If no zero-padding is selected, the voxel will be mirrored at the edges. An advantage of the mirroring is that it can give the effect of the voxel being surrounded by similarly dense vasculature [15].

RF pulses can be applied by defining the pulse axis in polar coordinates. The RF pulse orientation vector is defined as $[\theta, \phi]$, where θ is the polar angle and ϕ is the azimuthal angle relative to the x-direction. A 90° RF pulse oriented in the x-direction would then have an orientation vector $[\frac{\pi}{2}, 0]$ and a y-direction pulse would have the orientation vector $[\frac{\pi}{2}, \frac{\pi}{2}]$.

After voxel geometry definition and B_0 offset calculation, diffusion effects are simulated. This is modeled with Monte Carlo diffusion, which uses randomly generated particles that move through the voxel with a random walk. As implemented in BOLDswimsuite, the step length is calculated using a normal distribution, with standard deviation $\sqrt{2D\Delta t}$. D is the diffusion coefficient and Δt is the step in time length. Regardless of whether the voxel is continuous or discrete, the position of the diffusing particle is always calculated in continuous space. The advantage of doing it like this is that it allows for step sizes much smaller than

the grid elements to happen consecutively [15]. A visualization of the 3D random walk is shown below in figure 15.

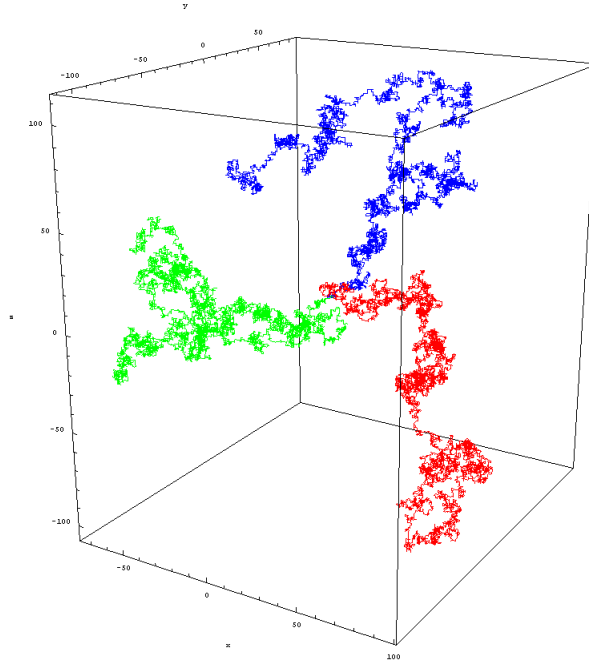


Figure 15: A depiction of the 3D random walk, with three different particles (red, blue, green) displaying possible random paths [16].

The boundary of voxels are defined periodically, meaning when a particle exits the voxel on one end, it reappears on the other. This allows for unrestricted diffusion while keeping the particle within the voxel's volume. A second boundary is defined at the surface of the perturbers within the voxel (i.e. 3D infinite-cylinders). When a particle nears the surface of a perturber there is a chance it successfully permeates the surface, given by the defined water permeation probability. The particle can either successfully permeate the surface and move to a new position, or generate a new step randomly until one is found that doesn't cross the surface boundary. At each step the particle accumulates phase, dependent on the magnetic field offset at its step position. In continuous voxels, the dephasing is calculated at each timestep. For discrete voxels, the dephasing is sampled from the grid of pre-calculated magnetic field offsets [15].

At each step of diffusion, the change in precessional frequency is determined by the equation below.

$$\Delta\omega = \gamma\Delta B_z \quad (13)$$

Where γ is the gyromagnetic ratio and ΔB_z is the magnetic field offset. The diffusing particle picks up additional phase at spin index p at each timestep due to the frequency shift. This is shown in the equation below.

$$\Delta\Phi(p) = \Delta\omega(p)\Delta t \quad (14)$$

Where Δt is the timestep. The resulting cumulative phase shift over all steps the diffusing particle takes is shown in the equation below.

$$\Phi(p) = \sum_{n=1}^{N_{steps}} \Delta\Phi(p_n) \quad (15)$$

The MR signal at each spin index p can then be found, shown below.

$$M_j(p) = e^{i\Phi(p)} \quad (16)$$

The total BOLD signal at a time point j is then found as the magnitude of the total MR signal over all spins in the voxel, shown below.

$$S_j = \sum_{p=1}^{N_{spins}} M_j(p) \quad (17)$$

Where S_j is the total BOLD signal [15].

3 Methods

This section outlines the simulation framework used to model voxel specific BOLD signal changes near large veins. It describes the modifications made to the `BOLD ω imsuite` toolbox, voxel construction and simulation parameter selection, and the process of voxel sub-sampling.

Figure 16 presents the region of interest used in simulation. A Pial vein is located near the cortical surface, generating large magnetic field offsets in the underlying tissue. Below this vein, a dense network of microvasculature is present. Biophysical simulations of this region were performed to evaluate the resulting BOLD signal in response to this configuration, with coloured squares representing the voxel sampling sizes used for signal analysis.

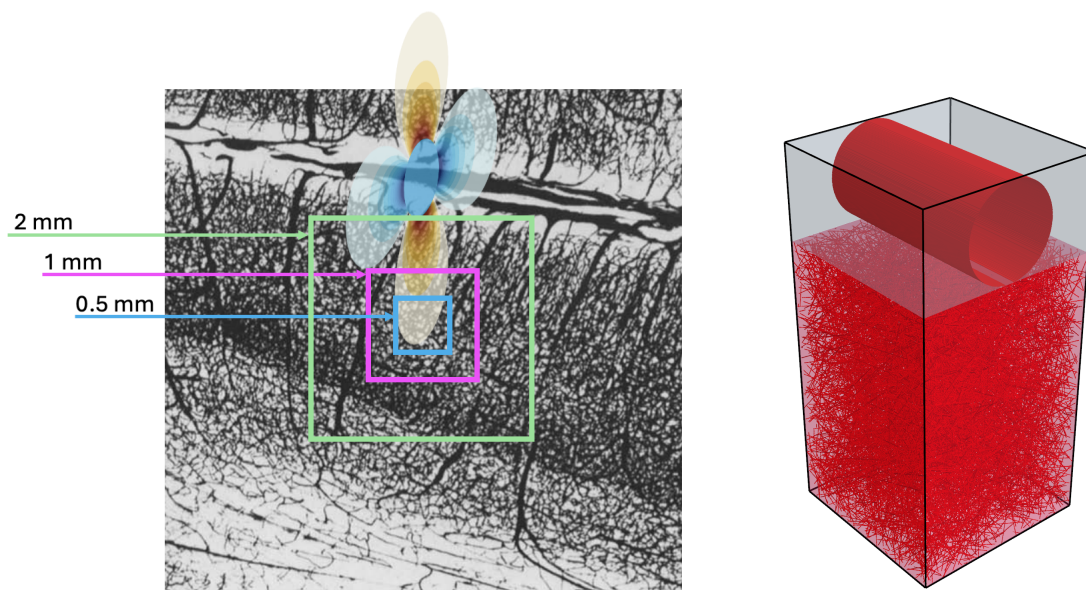


Figure 16: Simulation setup illustrating both the anatomical context (left) and computational voxel geometry (right) [37].

3.1 `BOLD ω imsuite` Toolbox Modifications

Several modifications were made to the `BOLD ω imsuite` toolbox to enable the simulation of a large pial vein and the surrounding microvasculature.

3.1.1 Tissue Index

Support for tissue boundaries was implemented to allow for region-specific T2 values within a single voxel. This capability allows for the modeling of the interface between cerebrospinal fluid (CSF), which surrounds the pial vein, and the underlying cortical tissue, containing the microvascular network. The flowchart shown in Figure 17 represents the pipeline added to generate the tissue index.

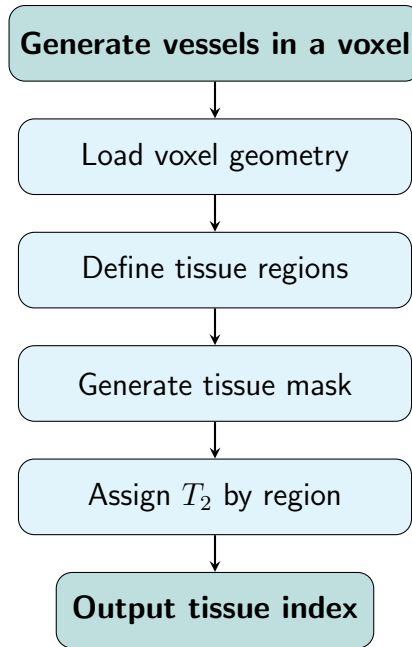


Figure 17: Pipeline for generating a tissue index grid from voxel geometry. This process enables spatially distinct assignment of T_2 values for simulating CSF and cortical tissue.

The resulting tissue index represents a 3D map, allowing for n tissue regions. Each individual region in the index holds a separate, user defined, T_2 . A visualization of the tissue index is shown below in Figure 18, with separately coloured regions representing a different tissue type.

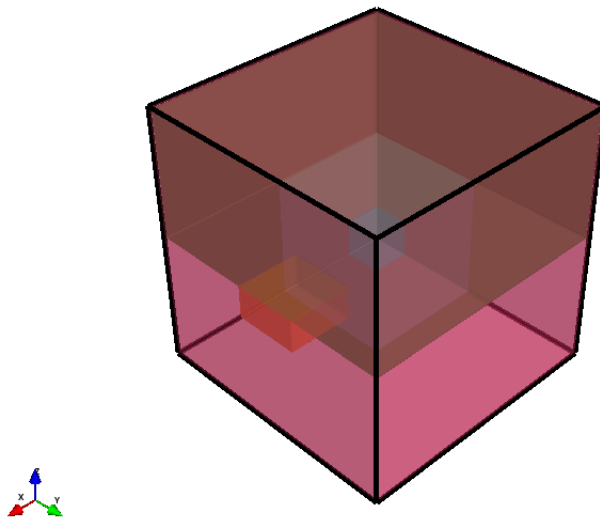


Figure 18: A visual representation of the tissue index, with highlighted regions representing a separate tissue type with a different T_2 value.

3.1.2 Anisotropic Voxel Sizes

The original BOLD ω imsuite framework supported only isotropic voxel dimensions. To increase flexibility, the code was modified to allow for generation of anisotropic voxels. This allowed an increase in allowed signal simulation depth, without an unnecessary increase in computational demand.

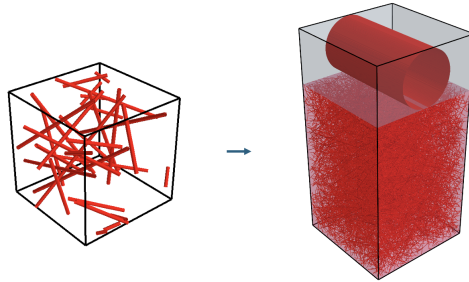


Figure 19: A comparison between an isotropic and anisotropic voxel, displaying the ability to generate non-cubic voxels.

3.1.3 Sub-Voxel Sampling

In BOLD ω imsuite, gradient echo sequences are modeled by applying a single RF pulse and tracking the subsequent signal decay. The imaging gradients used to form echoes in actual MR acquisitions are not explicitly modeled. As a result, the simulated signal reflects the decay of transverse magnetization following excitation.

To facilitate high-resolution analysis of local BOLD signal variations, a method within BOLD ω imsuite was defined to allow for signal simulation in sub-regions of a predefined parent voxel. The flowchart in Figure 20 represents the sub-voxel sampling pipeline.

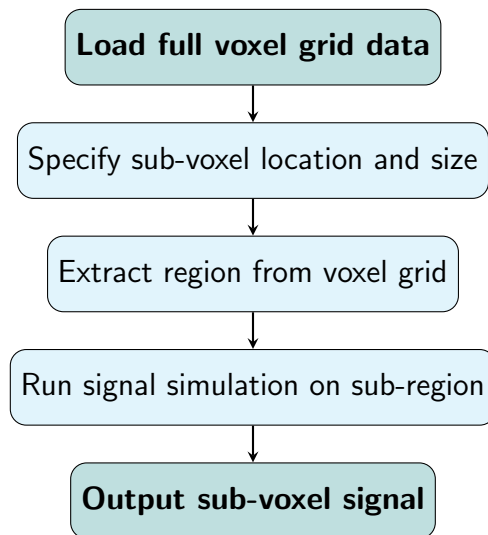


Figure 20: Pipeline for sub-voxel signal sampling. This method allows targeted simulation of signal evolution in user-defined subregions of the voxel to isolate local signal behaviour.

A region of interest is defined in the parent voxel. This region is sent through the signal simulation pipeline, returning signal calculated in the subregion. This method can then be looped to rapidly sample many sub-regions in the parent voxel. Figure 21 below shows the sampling of a sub-voxel from a predefined voxel containing multiple vessel sizes and tissues. The vessel index, magnetic field offsets, and tissue index are taken from the region of interest and a new voxel is generated, preserving region specific T_2 values from the parent voxel.

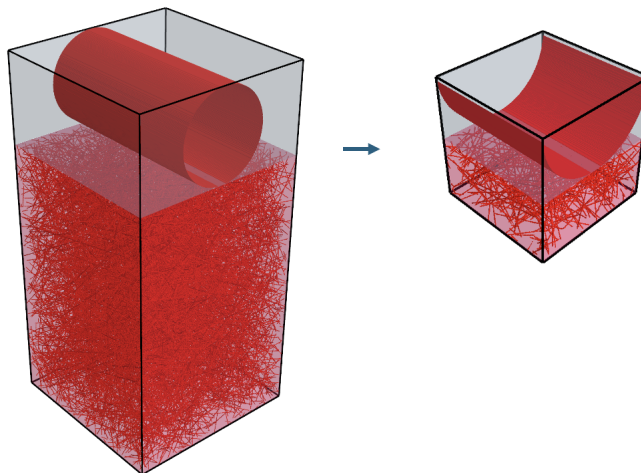


Figure 21: A sub-voxel (right) sampled from a parent voxel (left), sampled at the tissue boundary between the Pial vein and microvasculature.

3.2 Simulation Building

To generate a simulation of the pial vein and microvasculature, two voxels were generated separately and then combined.

The microvasculature was constructed first using the `from_random()` method in the `BOLDswimsuite` toolbox. This method accepts user defined parameters, including target cerebral blood volume (CBV), the magnetic susceptibility difference ($\Delta\chi$) between blood and tissue, the vessel diameter, and the size of voxel. The method populates a spherical region centered within the voxel's longest axis with randomly oriented cylindrical vessels, continuing until the specified CBV threshold is reached.

For this simulation, the initial continuous voxel was defined with dimensions of (2, 2, 3) mm. To align with the size of the final simulation, it was discretized with a resolution of (600, 600, 1200) and reshaped to a size of (2, 2, 4) mm using the `from_continuous_index_grid()` method. A cutoff height of 3 mm was applied to this voxel using a binary mask, eliminating all vessel indices above the cutoff to ensure no vessels appeared in the region allocated to the pial vein.

Following voxel construction, a discrete Fourier transform was applied to compute the magnetic field offsets induced by the vessel geometry under a 7 T static magnetic field. An FFT was used to calculate the magnetic field offset map to allow for increased realism at boundaries. The wraparound effects from excluding zero-padding simulate magnetic field offset from neighbouring vessels outside of the voxel. This also allows for a more accurate

simulation of magnetic field offsets at the pial boundary, as issues arising from analytical calculation forced a field cutoff directly at this boundary. An offset field cutoff was applied 0.25 mm from the top of the voxel to avoid wraparound effects from signal at the bottom of the voxel. Figure 22 below shows both the discretized voxel and its corresponding magnetic field offset map.

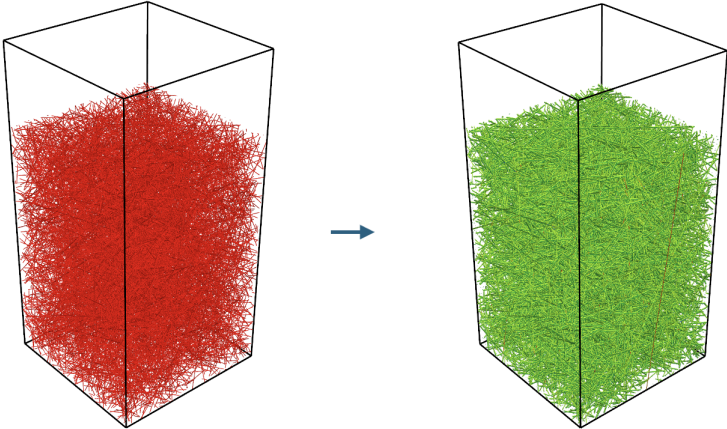


Figure 22: The discretized microvasculature voxel (left) and its corresponding magnetic field offset map (right).

Subsequently, a second voxel of size $(2, 2, 4)$ mm was generated to model the pial vein. A single 3D infinite cylinder with a diameter of 1 mm was positioned at the top of the voxel, aligned along the y-axis. The base of the cylinder was positioned directly on the tissue boundary to mimic the anatomical location of the pial vein. In this case, magnetic field offsets were computed analytically, allowing for direct discretization of the voxel and its corresponding magnetic offset field map at a resolution of $(600, 600, 1200)$. Figure 23 shows both the discretized pial vein voxel and its corresponding magnetic field offset map.

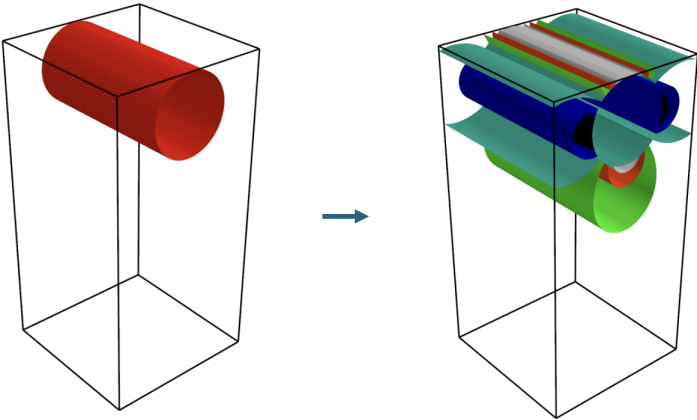


Figure 23: The discretized pial vein voxel (left) and its corresponding magnetic field offset map (right).

As both voxels were now discretized to a resolution of (600,600,1200) and the same size, (2,2,4) mm, their vessel indices and magnetic field offset maps were combined to create the final voxel. A tissue index grid was generated to simulate the tissue boundary between the pial vein and microvasculature, resulting in the final voxel shown below in figure 24.

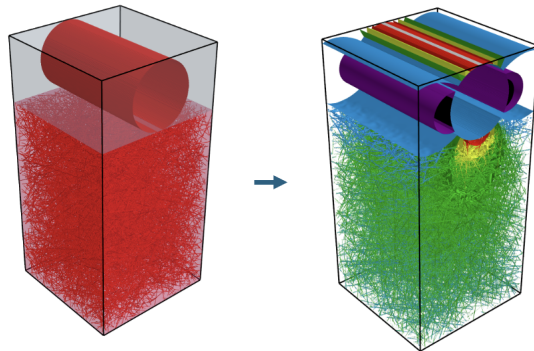


Figure 24: The discretized voxel (left), with tissue index map displaying the CSF (grey/blue) and the cortical tissue (light red), as well as its corresponding magnetic field offset map (right).

This was then repeated twice using pial diameters of 0.5 mm and 0.1 mm, resulting in three voxels, shown below.

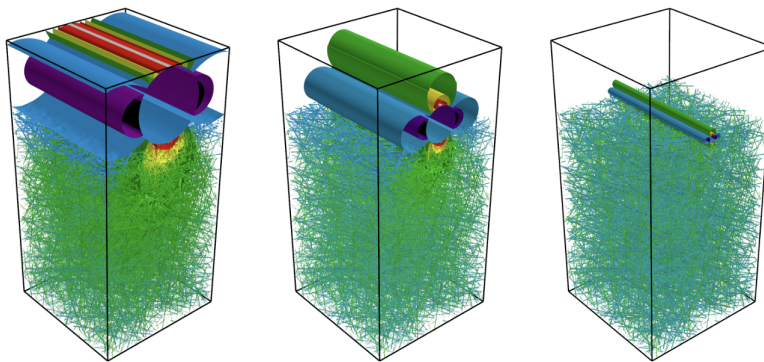


Figure 25: Simulated voxel with 1 mm pial vein (left), 0.5 mm pial vein (middle), and 0.1 mm pial vein (right).

3.2.1 Simulation parameters

Magnetic susceptibility for both the activated and baseline state were calculated with the equation below.

$$\Delta\chi = \Delta\chi_{do} \text{Hct} (1 - \text{SO}_2)$$

Where $\Delta\chi$ is the magnetic susceptibility difference between the intra- and extravascular space, $\Delta\chi_{do}$ is the intrinsic magnetic susceptibility difference between oxygenated and deoxygenated blood ($\Delta\chi_{do} = 0.264 \times 10^{-6}$), Hct is the Hematocrit, or fraction of blood volume

occupied by red blood cells, and SO_2 is the oxygen saturation, or fraction of blood cells that are oxygenated.

Intra- and extra-vascular T_2 values are calculated with the following equations, using the empirical formulae from Uludag et al., NeuroImage (2009).

Intra-vascular T_2 is found by calculating:

$$\begin{aligned} R_{2,0} &= 2.47 \text{ (s}^{-1}/T) \times B_0 - 0.6 \text{ (s}^{-1}) \\ R_{2,Hb,in} &= 12.67 \text{ (s}^{-1}/T^2) \times B_0^2 \times (1 - SO_2)^2 \\ R_{2,blood} &= R_{2,0} + R_{2,Hb,in} \\ T_{2,IV} &= \frac{1}{R_{2,blood}} \end{aligned}$$

Where $T_{2,IV}$ is the intra-vascular relaxation time, $R_{2,blood}$ is the total transverse relaxation rate of blood, $R_{2,0}$ represents the baseline relaxation rate independent of oxygenation, and $R_{2,Hb,in}$ accounts for the additional relaxation due to the presence of deoxyhemoglobin, which depends on both magnetic field strength (B_0) and blood oxygenation level (SO_2).

Extra-vascular T_2 is found by calculating:

$$\begin{aligned} R_2 &= 1.74 \text{ (s}^{-1}/T) \times B_0 + 7.77 \text{ (s}^{-1}) \\ T_{2,EV} &= \frac{1}{R_2} \end{aligned}$$

Where $T_{2,EV}$ is the extra-vascular relaxation time and R_2 is the corresponding transverse relaxation rate, which increases linearly with magnetic field strength B_0 .

Simulation of the signal of both the baseline and activated states for the pial vein and capillaries was performed using the simulation parameters below.

Parameter	Capillaries	Pial Vein
SO_2 (Baseline)	77.5%	60%
SO_2 (Activation)	85%	70%
Hct	0.33	0.44
Extravascular T_2	0.050 s	1.42 s
Intravascular T_2 (Baseline)	0.00639 s	0.00377 s
Intravascular T_2 (Activation)	0.00911 s	0.00493 s
Diameter	8 μm	1 mm, 0.5 mm, 0.1 mm
Sub-voxel sampling sizes	0.5 mm, 1 mm, 2 mm	0.5 mm, 1 mm, 2 mm
CBV	2%	—

Table 1: Parameters used for signal simulations of capillaries and pial vein at a static field strength of $B_0 = 7$ T.

Note: at the time of simulation, the code base did not support separate intra-vascular T_2 values for different vessel types. As a result, a single representative value of ($T_{2,IV} = 0.00493s$) was used for intra-vascular locations, using an SO_2 value of 70% and magnetic field strength of 7T.

3.3 Sub-Voxel Sampling

To investigate localized BOLD signal variations as a function of depth, the parent voxel shown in Figure 24 was systematically sampled using the sub-voxel method described in Section 3.1.3. The initial sampling region was centered at the tissue boundary, with dimensions of (2, 2, 2) mm. Signal simulation was then performed for this subregion.

Following each simulation, the sub-voxel region was translated downward by 0.01 mm along the z-axis. At each step, the signal simulation was repeated, and the resulting signal was stored. This iterative sampling continued until the bottom edge of the sub-voxel intersected with the lower boundary of the parent voxel. This was then repeated for voxel sizes of (1, 1, 1) mm and (0.5, 0.5, 0.5) mm. Sub-voxel sampling was also performed on the voxels shown in Figure 22, the microvasculature only voxel, and Figure 23, pial vein only voxel, for use in percentage signal change calculations.

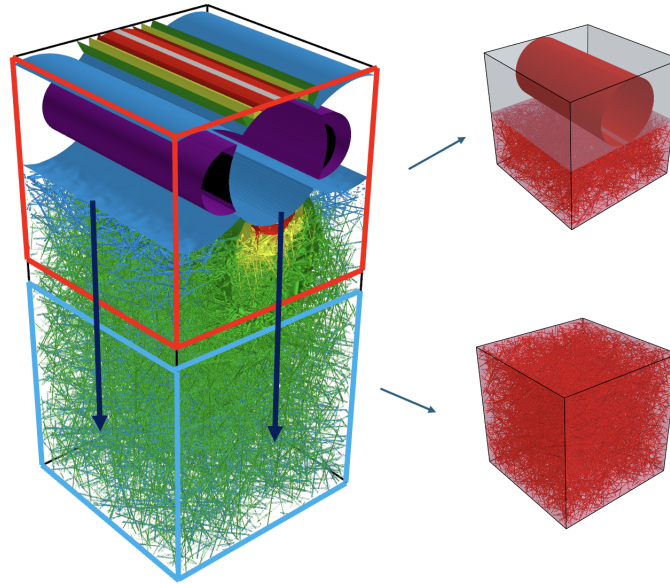


Figure 26: Illustration of the sub-voxel sampling procedure, showing the initial region at the tissue boundary and its downward translation.

4 Results

This section presents the results of signal simulations performed using the voxel configuration containing a $1000\ \mu\text{m}$ diameter pial vein. The analysis focuses on evaluating MR signal evolution as a function of cortical depth, with attention to the influence of large-vessel contamination on the measured MR signal originating from the underlying microvasculature. Data corresponding to simulations with $500\ \mu\text{m}$ and $100\ \mu\text{m}$ diameter pial veins are included in the appendices for comparison.

Following this, the BOLD signal between baseline and activated conditions is analyzed to determine the critical cortical depth at which the measured BOLD contrast predominantly reflects microvascular contributions rather than contamination from the pial vein.

4.1 Simulated Signal Visualization

Figures 27 and 28 show the simulated MR signal evolution across sub-voxel depths for the microvasculature-only voxel and the combined voxel containing both the pial vein and microvasculature, respectively. Each plot displays the MR signal for both baseline and activation conditions at multiple depths below the tissue boundary. In these plots, Cortical depth is shown with color intensity, with lighter shades of blue indicating regions closer to the pial surface (i.e., smaller cortical depths), and progressively darker shades representing deeper sub-voxel sampling regions further from the pial surface.

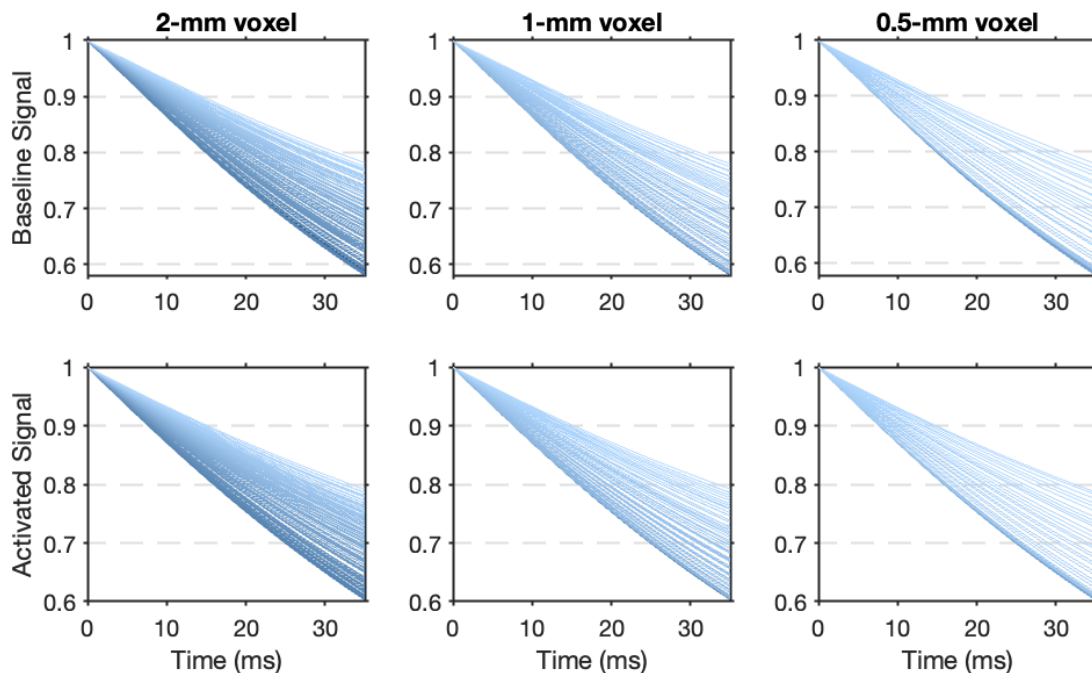


Figure 27: Gradient echo MR signal vs. time for the voxel containing only microvasculature. Signal is shown for various sub-voxel depths below the tissue boundary, for both baseline and activation conditions. Cortical depth is shown with lighter shades of blue indicating regions closer to the pial surface, and darker shades representing deeper sub-voxel sampling regions.

In the microvasculature-only case (Figure 27), an initial increase in signal dephasing is observed as additional microvasculature enters the voxel when moving from the empty space above the pial surface into the tissue. However, once the top of the voxel is fully below the pial surface, the signal decay becomes largely independent of depth due to the relatively uniform distribution of microvessels.

When the pial vein is introduced (Figure 28), a depth-dependent signal drop can be observed, with the strongest dephasing and signal loss occurring at low cortical depth. This is caused by large susceptibility-induced magnetic field inhomogeneities generated by the pial vein, which dominate near the surface and progressively weaken with depth. As a result, the inclusion of the pial vein introduces a strong depth-dependent gradient in signal dephasing that is not present in the microvascular-only simulations.

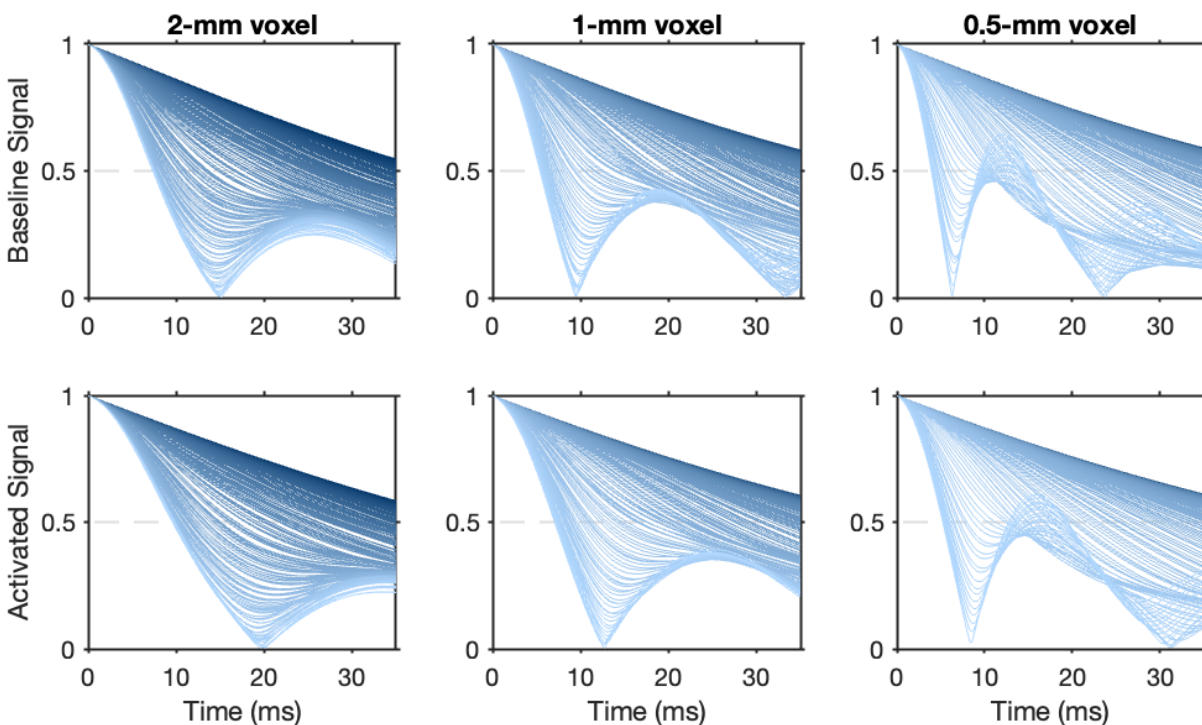


Figure 28: Gradient echo MR signal vs. time for the voxel containing both the pial vein and microvasculature. Signal is shown at varying depths below the tissue boundary, highlighting the influence of the large draining vein. Cortical depth is shown with lighter shades of blue indicating regions closer to the pial surface, and darker shades representing deeper sub-voxel sampling regions.

4.2 Signal Integration and Difference Plot

Signal was extracted at each cortical depth for both the combined voxel (containing the pial vein and microvasculature) and the vessel-only voxel (containing only microvasculature). An integration was then performed over time at each depth for each vessel configuration.

The integrated signal for each condition (cond), baseline and activation, was computed as:

$$I_{\text{comb}}^{(\text{cond})}(z) = \int_0^{35} S_{\text{comb}}^{(\text{cond})}(t, z) dt$$

$$I_{\text{vess}}^{(\text{cond})}(z) = \int_0^{35} S_{\text{vess}}^{(\text{cond})}(t, z) dt$$

Where $S_{\text{comb}}^{(\text{cond})}(t, z)$ is the signal at cortical depth z for the combined voxel and $I_{\text{comb}}^{(\text{cond})}(z)$ is the integral of that signal, or total area under the signal decay curve. Similarly, $S_{\text{vess}}^{(\text{cond})}(t, z)$ and $I_{\text{vess}}^{(\text{cond})}(z)$ correspond to the vessel-voxel. The integrated signal difference at each depth z is then defined as:

$$\Delta I^{(\text{cond})}(z) = \left(I_{\text{vess}}^{(\text{cond})}(z) - I_{\text{comb}}^{(\text{cond})}(z) \right)$$

Where $\Delta I^{(\text{cond})}(z)$ is the integrated signal difference, or difference in area under signal decay of the vessel-voxel and combined voxel.

These calculations were implemented in MATLAB using the `trapz()` function for numerical integration:

```

1  % Load signal data
2  comb_data = combined_data.d_1000.(condition).(shape_field);
3  vess_data = vessel_data.(condition).(shape_field);
4
5  signals_comb = comb_data.signals;
6  signals_vess = vess_data.signals;
7  time = comb_data.time;
8
9  num_depths = length(signals_comb);
10 z_vals = zeros(num_depths, 1);
11 integral_diff = zeros(num_depths, 1);
12
13 % Loop through each depth and compute the integrated signal difference
14 for i = 1:num_depths
15     eviv_comb = signals_comb{i}.eviv(mask); % Combined voxel signal
16     eviv_vess = signals_vess{i}.eviv(mask); % Vessel-only voxel signal
17
18     z_vals(i) = signals_comb{i}.z;
19
20     integral_diff(i) = trapz(time, eviv_vess) - trapz(time, eviv_comb);
21 end

```

The resulting integrated signal differences were plotted against cortical depth at three different sub-voxel sizes, to illustrate how the presence of the pial vein alters the integrated MR signal response across depth and voxel size, visualizing dephasing of signal.

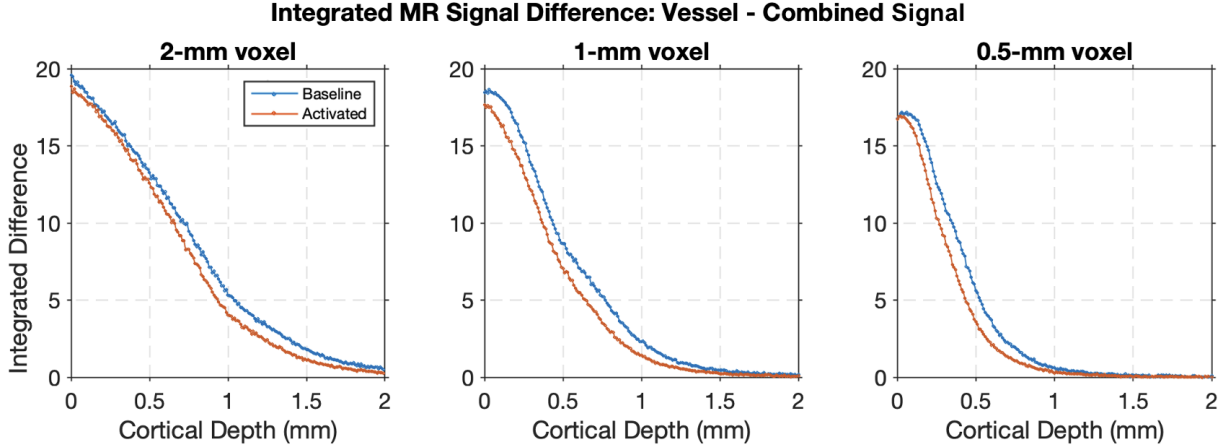


Figure 29: Integrated signal difference plots as a function of cortical depth for three different sub-voxel sizes.

These plots show a significant reduction in signal within the combined voxel near the cortical surface. As cortical depth increases, the magnitude of signal loss decreases, indicating reduced influence from the pial vein. It is also evident that smaller voxel sizes reduce dephasing more quickly, with signal difference approaching zero at shallower depths. Additionally, the activated signal exhibits reduced signal dephasing in all three scenarios, consistent with expectations due to increased oxygenation.

These results provide a measure of the impact of the pial vein on MR signal dephasing across cortical depth. By integrating the full signal decay curve rather than selecting a single echo time, this approach captures how much signal decay is introduced by the pial vein while removing sensitivity to noise and zeros that arise from natural rephasing effects. In particular, the integrated signal difference highlights the additional susceptibility effects caused by the pial vein, which dominate near the pial surface and progressively diminish with depth, providing a clearer depiction of depth-dependent signal loss.

4.3 Finding the Critical Depth

To evaluate the effect of activation within both the pial vein only voxel and microvasculature only voxel, the percent signal change was computed at a fixed signal sampling time of 25 ms, a typical TE for BOLD imaging at 7-T. For each cortical depth z , the percent change was calculated using the baseline and activated MR signal strength from the signal plots at $t = 25$ ms:

$$\text{Percent Change } (z) = 100 \times \left(\frac{S_{\text{pial}}^{(\text{baseline})}(t = 25\text{ms}, z) - S_{\text{pial}}^{(\text{activated})}(t = 25\text{ms}, z)}{S_{\text{pial}}^{(\text{activated})}(t = 25\text{ms}, z)} \right)$$

Where $S_{\text{pial}}^{(\text{baseline})}(t = 25\text{ms}, z)$ is the baseline signal from the pial only voxel evaluated at time $t = 25$ ms and cortical depth z , and $S_{\text{pial}}^{(\text{activated})}(t = 25\text{ms}, z)$ is the activated signal,

evaluated similarly.

This calculation was performed in MATLAB, with sample code calculating the percentage change in signal at all cortical depths for the simulated pial voxel signal below.

```
1 % Extract baseline and activated signal data for the pial vein voxel
2 pial_baseline = pial_data.d_1000.baseline.(shape_field);
3 pial_activated = pial_data.d_1000.activated.(shape_field);
4
5 baseline_signals_pial = pial_baseline.signals;
6 activated_signals_pial = pial_activated.signals;
7 time_array_pial = pial_baseline.time;
8
9 % Find index corresponding to 25 ms (closest match in time vector)
10 [~, idx_25ms] = min(abs(time_array_pial - 25));
11
12 % Preallocate arrays
13 n_depths = length(baseline_signals_pial);
14 z_vals_pial = zeros(n_depths, 1);
15 pct_change_pial = zeros(n_depths, 1);
16
17 % Loop through each depth and compute percent signal change at 25 ms
18 for i = 1:n_depths
19     z_vals_pial(i) = baseline_signals_pial{i}.z;
20     base_val = baseline_signals_pial{i}.eviv(idx_25ms);
21     act_val = activated_signals_pial{i}.eviv(idx_25ms);
22     pct_change_pial(i) = 100 * (base_val - act_val) / act_val;
23 end
24
25 % Convert depth values to cortical depth (distance from pial surface)
26 cortical_depths_pial = 1 - z_vals_pial;
27
28 % Sort depths and corresponding signal changes
29 [cortical_depths_pial_sorted, idx] = sort(cortical_depths_pial);
30 pct_change_pial_sorted = pct_change_pial(idx);
```

The percentage signal change calculation was then repeated for the microvasculature only voxel signal data. These calculations were performed on data from the (2,2,2) mm, (1,1,1) mm, and (0.5,0.5,0.5) mm sub-voxel datasets. Figure 30 below shows the resulting plot of % signal change as a function of cortical depth for each sub-voxel size.

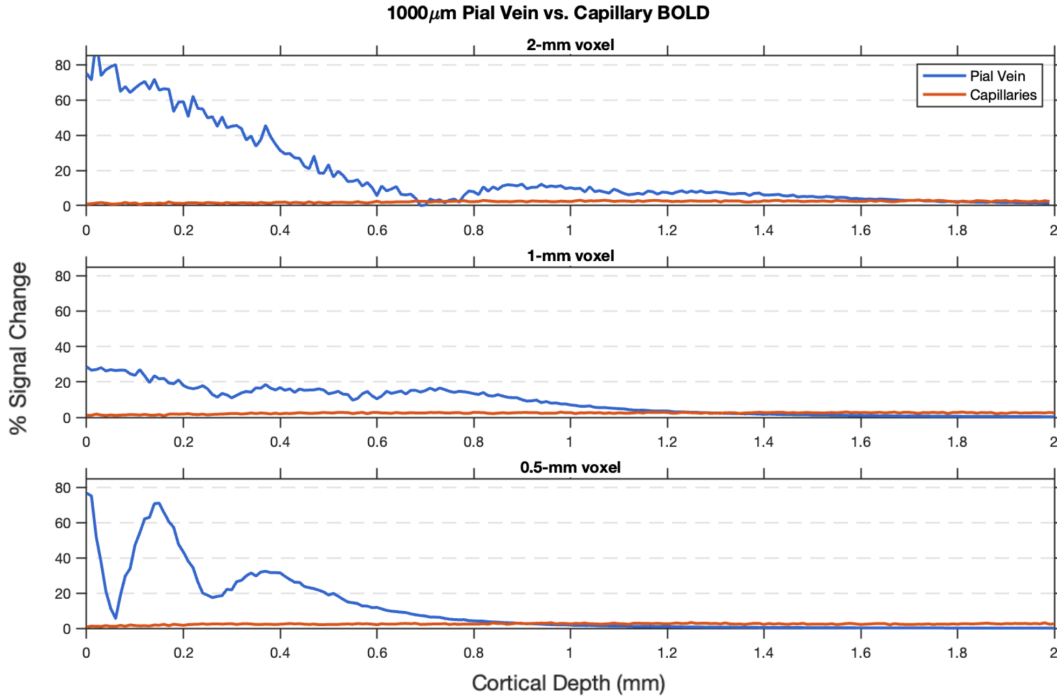


Figure 30: Percentage signal change of both the pial vein voxel and microvasculature voxel as a function of cortical depth, calculated at $t = 25$ ms. Three plots are shown for each the 2 mm, 1 mm, and 0.5 mm sub-voxel sampling sizes.

Following this, the critical cortical depth was identified, defined as the position where the percentage signal change from the microvasculature surpasses that of the pial vein.

To identify the critical depth, the difference in percentage signal change was computed as:

$$\Delta P(z) = P_{\text{pial}}(z) - P_{\text{micro}}(z)$$

where $P_{\text{pial}}(z)$ and $P_{\text{micro}}(z)$ are the percent signal changes at cortical depth z for the pial vein and microvasculature voxels, respectively.

To estimate the critical depth z_c where this difference crosses zero, linear interpolation was used between the cortical depths z_1 and z_2 , corresponding to the values immediately before and after the final sign change in the difference of percentage signal change from positive to negative:

$$z_c = z_1 - \Delta P(z_1) \cdot \frac{z_2 - z_1}{\Delta P(z_2) - \Delta P(z_1)}$$

This expression assumes that $\Delta P(z)$ varies linearly between z_1 and z_2 , allowing for estimation of the zero-crossing point that represents the critical depth.

This calculation was performed in MATLAB, with sample code calculating the critical depth shown below.

```

1 % Compute difference between microvascular and pial percentage signal
  change
2 diff_signal = pct_change_pial_sorted - pct_change_vessel_sorted;
3
4 % Identify where the sign of the difference crosses zero
5 sign_changes = find(diff(diff_signal > 0));
6
7 % If a crossover is found, interpolate to estimate the critical depth
8 if ~isempty(sign_changes)
9     last_idx = sign_changes(end);
10    x1 = cortical_depths_sorted(last_idx);
11    x2 = cortical_depths_sorted(last_idx + 1);
12    y1 = diff_signal(last_idx);
13    y2 = diff_signal(last_idx + 1);
14
15    % Linear interpolation to estimate the zero-crossing point
16    crit_depth = x1 - y1 * (x2 - x1) / (y2 - y1);
17    critical_depths(v, s) = crit_depth;
18 end

```

The resulting critical depths found using this calculation are shown below in table 2.

Voxel Size (mm)	1 mm Pial Vein	0.5 mm Pial Vein	0.1 mm Pial Vein
(2, 2, 2)	1.807 mm	1.283 mm	—
(1, 1, 1)	1.308 mm	0.883 mm	0.289 mm
(0.5, 0.5, 0.5)	0.899 mm	0.644 mm	0.265 mm

Table 2: Estimated critical cortical depths at which microvascular signal change surpasses pial vein contributions, for different voxel sizes and pial vein diameters.

The critical depths found corresponding to the 1000 μ m pial vein voxel were then plotted on the percentage signal change and cortical depth plot, shown below in figure 31. Following this, a bar chart plot was made to represent the relationship between critical depth, sub-voxel size, and pial vein diameter, shown below in figure 32.

For a 1000 μ m pial vein, the critical depth increased from approximately 0.9 mm at a (0.5, 0.5, 0.5) mm voxel size to about 1.8 mm at (2, 2, 2) mm. Similarly, for a 500 μ m vein, the critical depth ranged from roughly 0.6 mm to 1.3 mm, while the smallest vein (100 μ m) showed minimal contamination across all voxel sizes. Notably, at the (2, 2, 2) mm voxel size the percent signal change from the 100 μ m pial vein never exceeded that of the microvasculature.

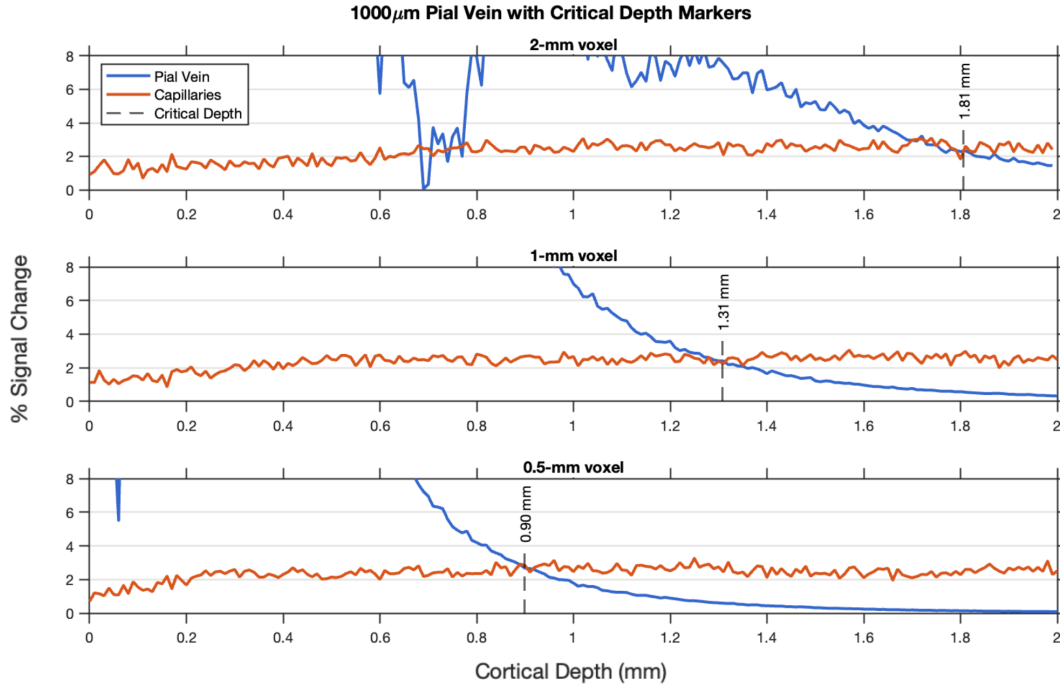


Figure 31: Percentage signal change of both the pial vein voxel and microvasculature voxel as a function of cortical depth, with vertical lines added representing the corresponding critical depths for each subplot.

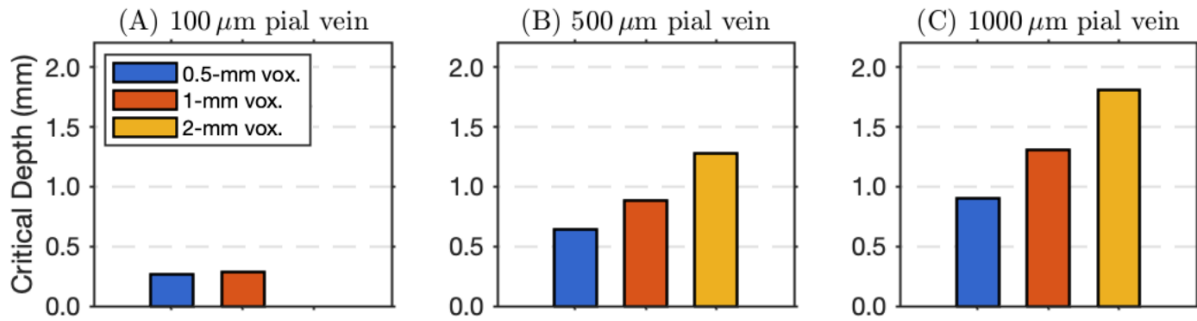


Figure 32: Bar plots of estimated critical cortical depth at which microvascular signal contributions exceed those from the pial vein, shown for each voxel size. Each subplot corresponds to a different pial vein diameter: 0.1 mm, 0.5 mm, and 1 mm (left to right).

A clear trend is observed in the bar plots of critical cortical depth: as voxel size increases, the critical depth at which microvascular signal overtakes pial vein contributions also increases. Likewise, increasing the diameter of the pial vein leads to a deeper critical depth. These results suggest that both larger voxel sizes and larger veins increase contamination in the measured BOLD signal, reinforcing the idea that smaller voxel sizes enable more accurate detection of microvascular-driven BOLD contrast.

5 Discussion

This study examined the influence of voxel size on the spatial specificity of BOLD fMRI signal near a large vein. Using BOLDswimsuite, signal contamination from a pial vein positioned above microvasculature was modeled, and the effect of voxel size on signal contamination from a large vein in BOLD fMRI at different cortical depths was evaluated.

The results demonstrate a clear dependence of signal contamination on both voxel size and pial vein diameter. In most cases, the presence of the large vein caused signal dephasing in nearby voxels, distorting the measured BOLD response and reducing its spatial specificity. However, with increasing cortical depth, the influence of the vein diminished, and the local BOLD signal began to more accurately reflect underlying microvascular activity.

While the current simulation toolbox is capturing the expected trends in large-vessel signal contamination, several limitations may affect the accuracy of the results. First, the use of 3D infinite cylinders to represent blood vessels neglects realistic vascular curvature, tapering, and branching, which are prominent features of cortical vasculature. This simplification may underestimate the spatial spread of magnetic field perturbations. Additionally, the use of a single, fixed intra-vascular T_2 across all vessel types and conditions may also suppress relevant differences in signal decay between capillaries and larger veins due to their difference in oxygen saturation.

Future work includes expanding on these findings by increasing the spatial resolution of simulations. Generating parent voxels at a (2000, 2000, 4000) grid resolution would provide 1 μm resolution, allowing for more precise modeling of vessels. Performing simulations with additional voxel sizes, pial vein sizes, and varying static magnetic field strengths would also help to generalize the observed trends. Signal readout could be improved by incorporating more realistic gradient echo readout models, such as varying echo times or modeling of imaging gradients. Pial vein orientation effects should also be evaluated, as these can significantly alter the spatial spread of field inhomogeneities. Finally, incorporating Vascular Anatomical Network (VAN)-style models could provide a more biologically accurate vascular geometry, including curvature, branching, and vessel density gradients across cortical depth [43].

6 Conclusion

This work investigated the impact of voxel size on BOLD fMRI signal contamination from large pial veins. Through biophysical simulations performed using the BOLDswimsuite toolbox, it was shown that large veins induce strong magnetic field offsets that heavily influence signal decay near the pial surface, with their effects progressively decreasing with depth. Smaller voxel sizes reduced the extent of contamination more rapidly, allowing for microvascular-specific BOLD contrast to be recovered at shallower cortical depths. Additionally, the presence of larger veins was found to push the critical depth deeper into the cortex. These results reinforce the importance of voxel size selection for achieving microvascular specificity in BOLD fMRI.

7 References

- [1] Mcrobbie, Donald W. MRI from Picture to Proton. Editorial: Cambridge, Cambridge University Press, 2007, sec. 3.2.
- [2] Mcrobbie, Donald W. MRI from Picture to Proton. Editorial: Cambridge, Cambridge University Press, 2007, sec. 3.1.
- [3] Mcrobbie, Donald W. MRI from Picture to Proton. Editorial: Cambridge, Cambridge University Press, 2007, sec. 3.7.
- [4] Mcrobbie, Donald W. MRI from Picture to Proton. Editorial: Cambridge, Cambridge University Press, 2007, fig. 3.10.
- [5] Mcrobbie, Donald W. MRI from Picture to Proton. Editorial: Cambridge, Cambridge University Press, 2007, sec. 3.4.
- [6] Mcrobbie, Donald W. MRI from Picture to Proton. Editorial: Cambridge, Cambridge University Press, 2007, sec. 7.2.
- [7] Mcrobbie, Donald W. MRI from Picture to Proton. Editorial: Cambridge, Cambridge University Press, 2007, fig. 8.4.
- [8] Mcrobbie, Donald W. MRI from Picture to Proton. Editorial: Cambridge, Cambridge University Press, 2007, fig. 8.6.
- [9] Mcrobbie, Donald W. MRI from Picture to Proton. Editorial: Cambridge, Cambridge University Press, 2007, sec. 8.2.
- [10] Mcrobbie, Donald W. MRI from Picture to Proton. Editorial: Cambridge, Cambridge University Press, 2007, sec. 8.3.
- [11] Mcrobbie, Donald W. MRI from Picture to Proton. Editorial: Cambridge, Cambridge University Press, 2007, sec. 8.4.
- [12] Mcrobbie, Donald W. MRI from Picture to Proton. Editorial: Cambridge, Cambridge University Press, 2007, fig. 8.9.
- [13] Mcrobbie, Donald W. MRI from Picture to Proton. Editorial: Cambridge, Cambridge University Press, 2007, sec. 16.5.1.
- [14] Mcrobbie, Donald W. MRI from Picture to Proton. Editorial: Cambridge, Cambridge University Press, 2007, sec. 16.5.6.
- [15] Chausse, J., Berman, A. J. L., & Chen, J. J. (2025). BOLD_swimsuite: A new software suite for forward modeling of the BOLD fMRI signal. *Imaging Neuroscience*. https://doi.org/10.1162/imag_a_00519

- [16] “File:Walk3d 0.Png - Wikipedia.” Wikipedia.org, 2020, en.m.wikipedia.org/wiki/File:Walk3d_0.png.
- [17] Berman, A. J. L., Balasubramanian, M., Setsompop, K., & Polimeni, J. R. (2024). *Small voxel sizes reduce extravascular dephasing from large veins in gradient-echo BOLD fMRI at 7T: a simulation study*. In *Proc. Intl. Soc. Mag. Reson. Med. 32 (2024)*
- [18] Berman, A., Balasubramanian, M., Setsompop, K., & Polimeni, J. (2024). Small voxel sizes reduce large-vein effects and extravascular dephasing in gradient-echo BOLD at 7T: a simulation study [Conference presentation]. fig. slide 7.
- [19] “Relaxation Times and Basic Pulse Sequences • Magnetic Resonance in Medicine – the Basics – by Peter A. Rinck — NMR MR MRI — Essentials, Introduction, Basic Principles, Facts, History — the Primer of EMRF/TRTF.” Magnetic-Resonance.org, 2024, magnetic-resonance.org/ch/04-04.html.
- [20] Berman, A., Balasubramanian, M., Setsompop, K., & Polimeni, J. (2024). Small voxel sizes reduce large-vein effects and extravascular dephasing in gradient-echo BOLD at 7T: a simulation study [Conference presentation]. fig. slide 4.
- [21] Mcrobbie, Donald W. MRI from Picture to Proton. Editorial: Cambridge, Cambridge University Press, 2007, sec. 7.4.
- [22] Mcrobbie, Donald W. MRI from Picture to Proton. Editorial: Cambridge, Cambridge University Press, 2007, sec. 6.8.
- [23] Brown, Robert W, et al. Magnetic Resonance Imaging : Physical Principles and Sequence Design. Hoboken, New Jersey, John Wiley & Sons, Inc, 1999. sec. 2.2.3.
- [24] Berman, A. J. L. *Development of a Functional Magnetic Resonance Imaging Simulator: Deterministic Simulation of the Transverse Magnetization in Microvasculature*. MSc thesis, Medical Physics Unit, McGill University, 2012, sec.2.1.2.
- [25] Mcrobbie, Donald W. MRI from Picture to Proton. Editorial: Cambridge, Cambridge University Press, 2007, fig. 4.7.
- [26] Mcrobbie, Donald W. MRI from Picture to Proton. Editorial: Cambridge, Cambridge University Press, 2007, sec. 4.3.
- [27] Mcrobbie, Donald W. MRI from Picture to Proton. Editorial: Cambridge, Cambridge University Press, 2007, sec. 7.5.2.
- [28] Mcrobbie, Donald W. MRI from Picture to Proton. Editorial: Cambridge, Cambridge University Press, 2007, sec. 4.6.
- [29] Mcrobbie, Donald W. MRI from Picture to Proton. Editorial: Cambridge, Cambridge University Press, 2007, fig. 4.12.
- [30] Mcrobbie, Donald W. MRI from Picture to Proton. Editorial: Cambridge, Cambridge University Press, 2007, sec. 5.3.

- [31] McRobbie, Donald W. MRI from Picture to Proton. Editorial: Cambridge, Cambridge University Press, 2007, sec. 11.3.
- [32] McRobbie, Donald W. MRI from Picture to Proton. Editorial: Cambridge, Cambridge University Press, 2007, fig. 16.18.
- [33] Berman, A. J. L. (2022). *Improved functional MRI acquisition and modelling for imaging brain function and physiology*. In *OMPI Seminar Series*, fig. slide 12.
- [34] Ogawa, S., et al. “Functional Brain Mapping by Blood Oxygenation Level-Dependent Contrast Magnetic Resonance Imaging. A Comparison of Signal Characteristics with a Biophysical Model.” *Biophysical Journal*, vol. 64, no. 3, Mar. 1993, pp. 803–812, [https://doi.org/10.1016/s0006-3495\(93\)81441-3](https://doi.org/10.1016/s0006-3495(93)81441-3).
- [35] Boxerman JL, Hamberg LM, Rosen BR, Weisskoff RM. MR Contrast Due to Intravascular Magnetic-Susceptibility Perturbations. *Magn Reson Med* 1995;34(4):555-566.
- [36] Berman, A.J.L. *Advancing Calibrated Functional MRI Through Biophysical Signal Modelling*. PhD Thesis, McGill University, Department of Biomedical Engineering, 2017.
- [37] Duvernoy, H.M., et al. “Cortical Blood Vessels of the Human Brain.” *Brain Research Bulletin*, vol. 7, no. 5, Nov. 1981, pp. 519–579, [https://doi.org/10.1016/0361-9230\(81\)90007-1](https://doi.org/10.1016/0361-9230(81)90007-1).
- [38] “T1 Relaxation.” *Questions and Answers in MRI*, 2024, mriquestions.com/what-is-t1.html.
- [39] “T2 (Spin-Spin) Relaxation.” *Questions and Answers in MRI*, 2024, mriquestions.com/what-is-t2.html.
- [40] Wald, Lawrence L. “The Future of Acquisition Speed, Coverage, Sensitivity, and Resolution.” *NeuroImage*, vol. 62, no. 2, Aug. 2012, pp. 1221–1229, <https://doi.org/10.1016/j.neuroimage.2012.02.077>.
- [41] Reichenbach, Jürgen R., et al. “Theory and Application of Static Field Inhomogeneity Effects in Gradient-Echo Imaging.” *Journal of Magnetic Resonance Imaging*, vol. 7, no. 2, Mar. 1997, pp. 266–279, <https://doi.org/10.1002/jmri.1880070203>.
- [42] Uğurbil, Kamil. “Ultrahigh Field and Ultrahigh Resolution fMRI.” *Current Opinion in Biomedical Engineering*, Apr. 2021, p. 100288, <https://doi.org/10.1016/j.cobme.2021.100288>.
- [43] Gagnon, Louise, et al. “Quantifying the Microvascular Origin of BOLD-fMRI from First Principles with Two-Photon Microscopy and an Oxygen-Sensitive Nanoprobe.” *The Journal of Neuroscience*, vol. 35, no. 8, 25 Feb. 2015, pp. 3663–3675, <https://doi.org/10.1523/jneurosci.3555-14.2015>.
- [44] Berman AJL, Grissom WA, Witzel T, et al. Ultra-high spatial resolution BOLD fMRI in humans using combined segmented- accelerated VFA-FLEET with a recursive RF pulse design. *Magn Reson Med*. 2020;00:1–20. <https://doi.org/10.1002/mrm.28415>

8 Appendices

8.1 Signal Plots

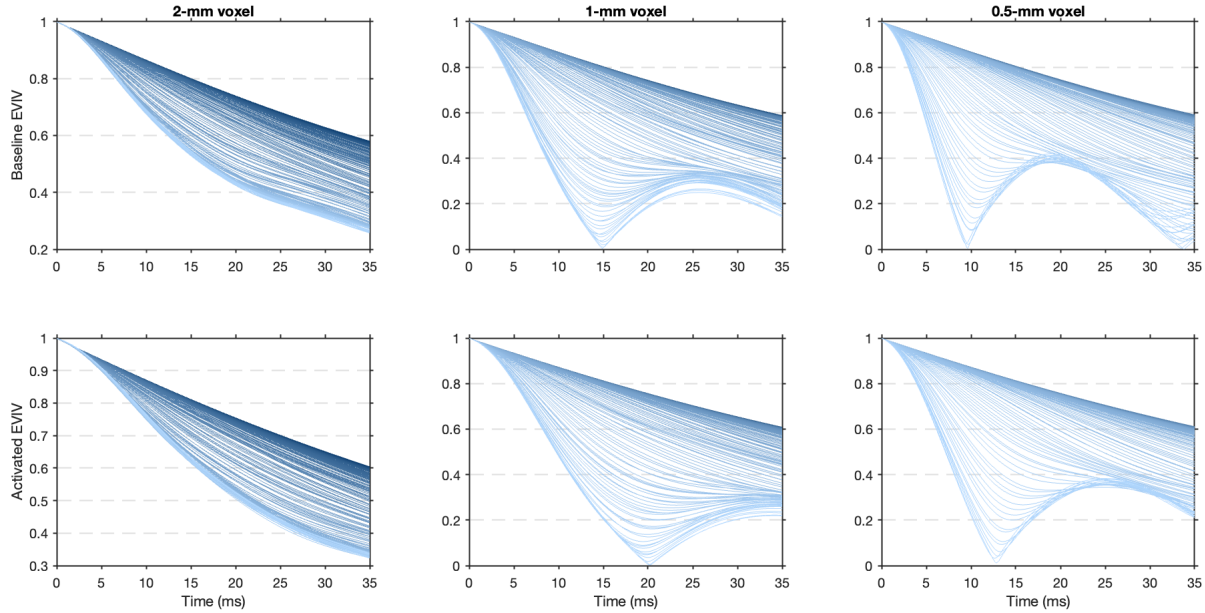


Figure 33: Gradient echo MR signal vs. time for the voxel containing both the pial vein and microvasculature. Data here is collected using the 500 μ m pial vein combined voxel.

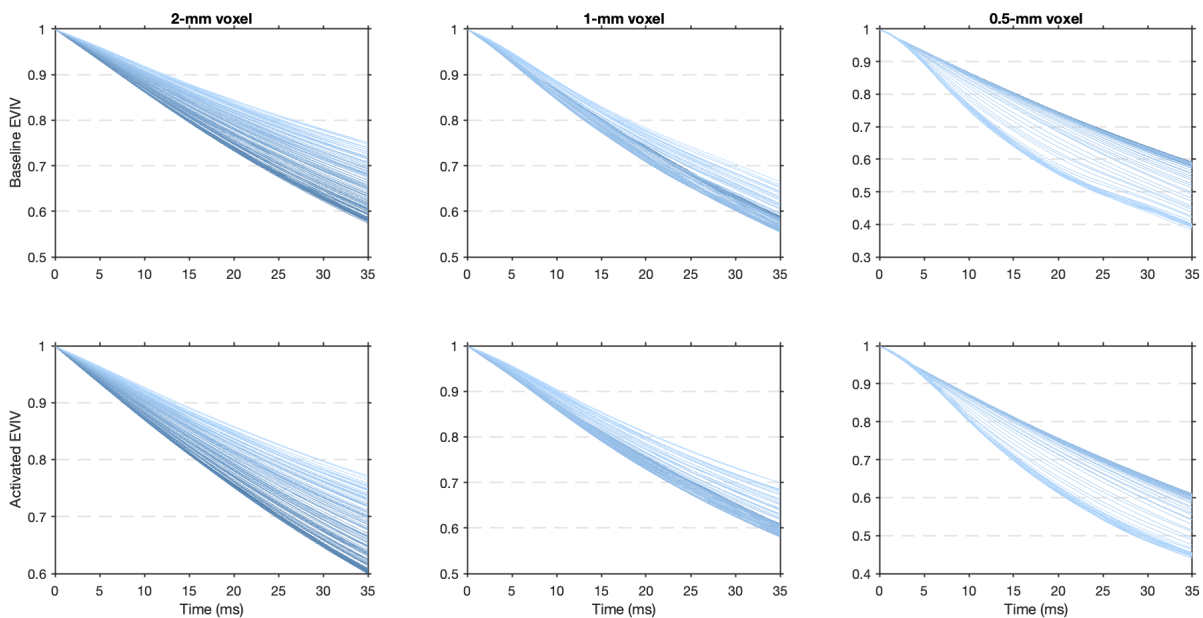


Figure 34: Gradient echo MR signal vs. time for the voxel containing both the pial vein and microvasculature. Data here is collected using the 100 μ m pial vein combined voxel.

8.2 Integral Plots

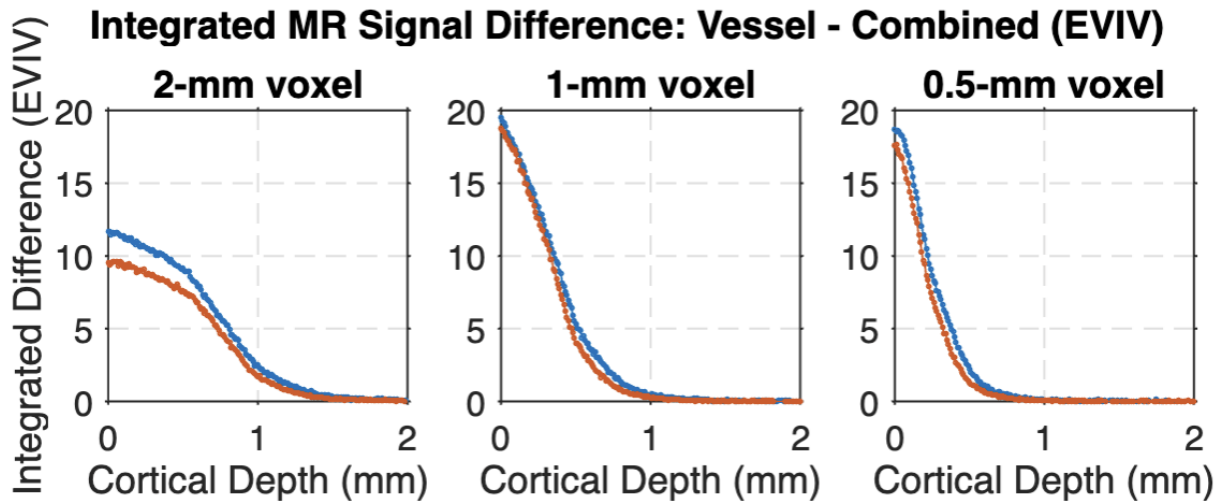


Figure 35: Integrated signal difference plots as a function of cortical depth for three different sub-voxel sizes, using a pial diameter of 500 μ m.

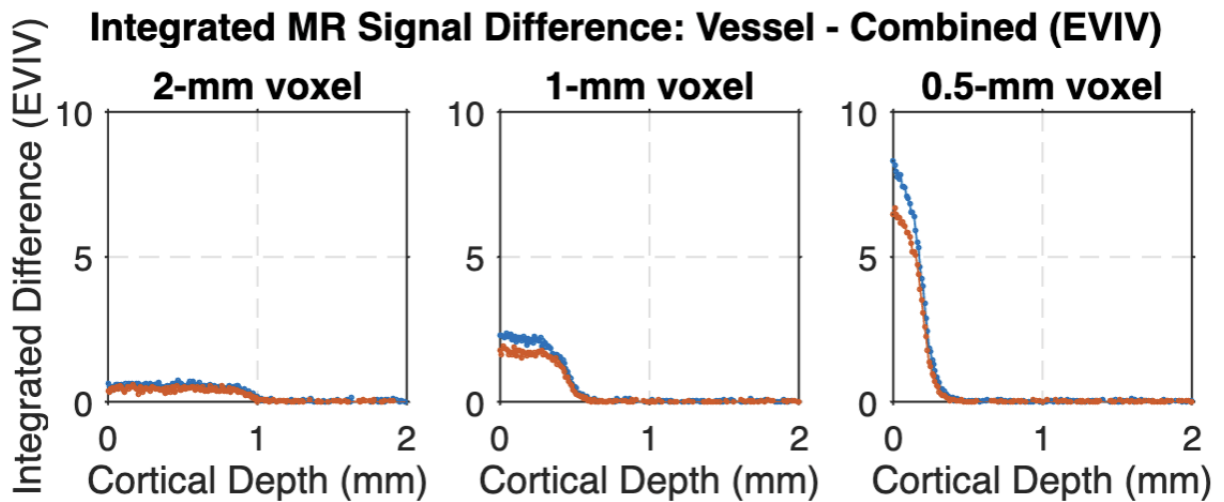


Figure 36: Integrated signal difference plots as a function of cortical depth for three different sub-voxel sizes, using a pial diameter of 100 μ m.

8.3 Percent Signal Change Plots

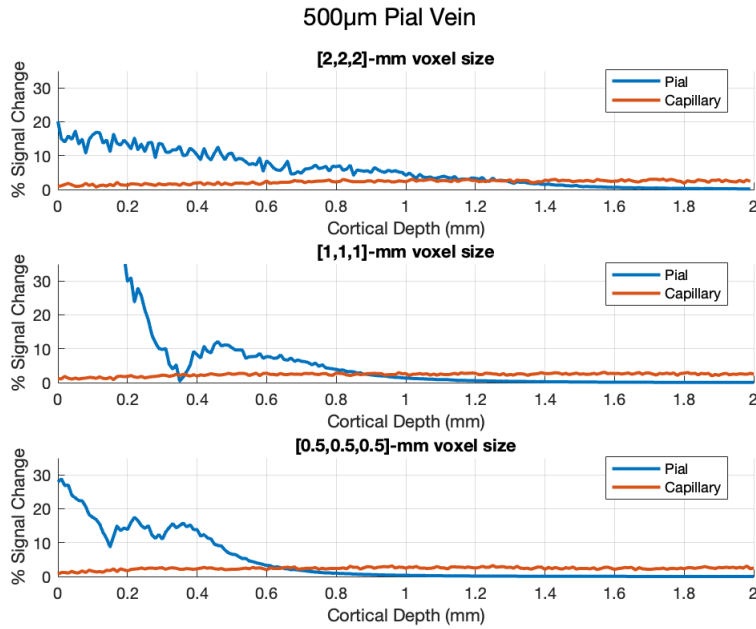


Figure 37: Percentage signal change of both the pial vein voxel and microvasculature voxel as a function of cortical depth. Data here is collected using the 500µm pial vein diameter.

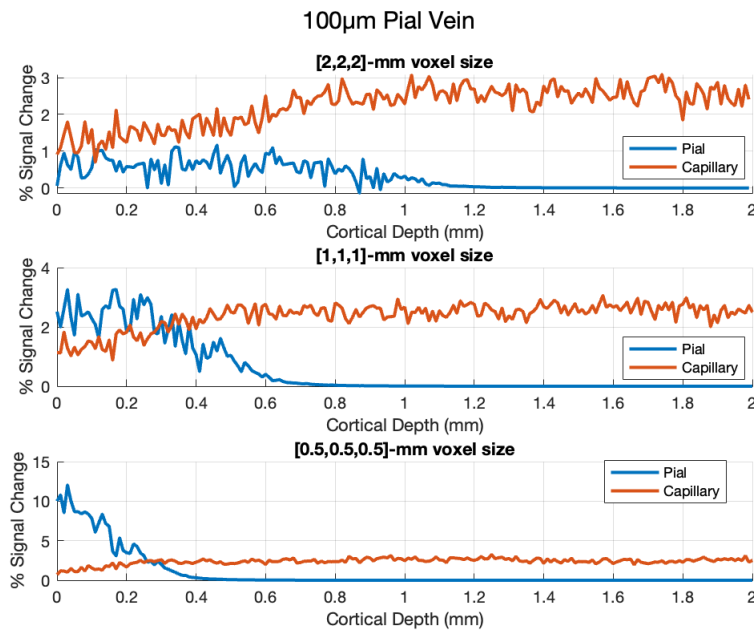


Figure 38: Percentage signal change of both the pial vein voxel and microvasculature voxel as a function of cortical depth. Data here is collected using the 100µm pial vein diameter.

8.4 Critical Depth Plots

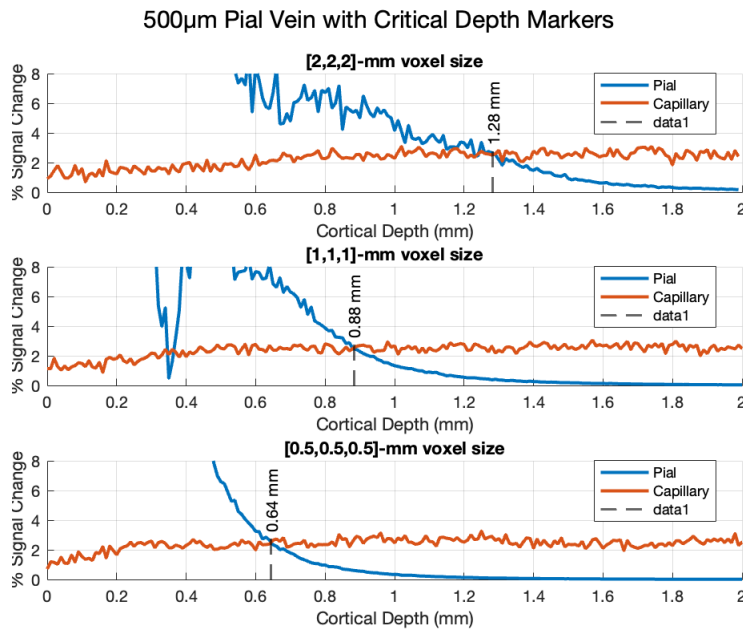


Figure 39: Percentage signal change of both the pial vein voxel and microvasculature voxel as a function of cortical depth, with vertical lines added representing the corresponding critical depths for each subplot. Data here is collected using the 500 μ m pial vein diameter.

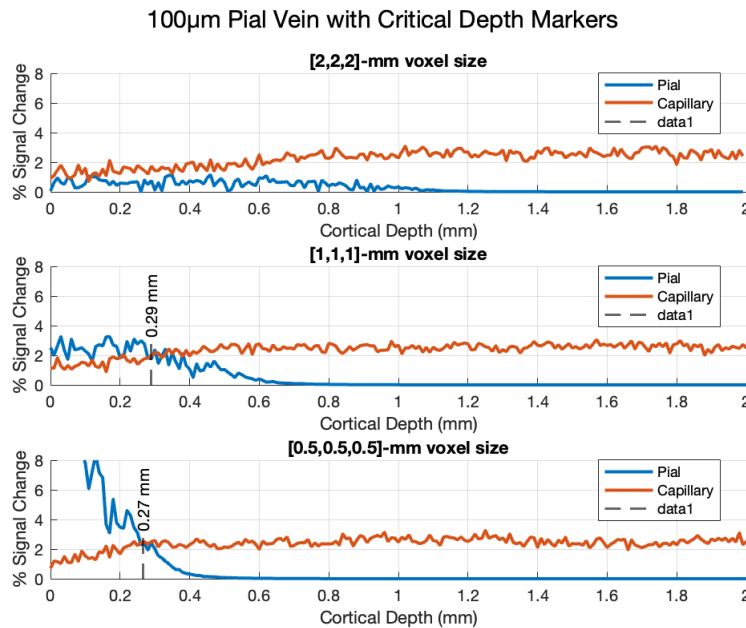


Figure 40: Percentage signal change of both the pial vein voxel and microvasculature voxel as a function of cortical depth, with vertical lines added representing the corresponding critical depths for each subplot. Data here is collected using the 100 μ m pial vein diameter.